An Asymmetrical Phase-Shift Scheme of Three-Phase Dual Active Bridge With Minimum Current Root-Mean-Square Value Control

Hui Chen, *Student Member, IEEE*, Shaodi Ouyang, *Member, IEEE*, Jinjun Liu, *Fellow, IEEE*, and Xianzao Li, *Student Member, IEEE*

***Abstract*—The three-phase dual active bridge (3ph-DAB) converter is a promising topology attracting increasing attention. However, because it is limited to symmetrical three-phase bridge control, the conventional single-phase-shift control method (SPS) remains the most common method for 3ph-DAB converter. The obvious shortcomings of SPS control include the soft-switching failure, massive circulating energy, and high root-mean-square (rms) current value at the light load, particularly with large voltage variation-ratio conditions. To overcome these drawbacks, this article proposes a novel asymmetrical phase shift (APS) control strategy. Unlike other optimized modulation schemes, this optimized strategy breaks the symmetrical control rules of three-phase bridges by introducing variable phase-shift angles among three-phase legs. The novel APS control strategy can substantially reduce the current's rms value and extend the soft-switching operation range due to these additional phase-shift angles. Further, the analytical solutions for the optimal phase-shift angles are derived by solving the global optimal condition equations. Analytical solutions, compared with complex numerical solutions derived by other optimized schemes, can be easily adopted in digital implementation and perform well under changing parameter conditions. Finally, experimental results verify the outstanding performance of the proposed modulation strategy.**

***Index Terms*—Analytical solutions, asymmetrical phase shift (APS) control, optimized modulation strategy, reduction of current's root-mean-square (rms) value, soft switching, the global optimal condition (GOC) equations, three-phase dual active bridge (3ph-DAB).**

I. Introduction

With the advancement of power electronics, the high-power and frequency isolated bidirectional dc/dc converter (IBDC) has become a popular converter in high-power industrial applications, such as hybrid energy storage systems, electrical vehicle power systems, data center power supplies, solid-state transformers, and distributed direct current (dc) microgrid [1]–[4], [33], [34]. In the IBDC family, the single-phase dual active bridge (1ph-DAB) is one of the well-known topologies proposed in [5]. This converter is widely used in industrial applications due to its bidirectional power flowing capability, buck–boost voltage characteristics, inherent soft-switching operation, and simple control method. The three-phase dual active bridge converter (3ph-DAB) is the preferred choice for high-power applications compared with the 1ph-DAB. 3ph-DAB inherits the advantages of 1ph-DAB and it has the additional superiorities to transfer higher power with lower root-mean-square (rms) current, smaller component stress, and higher power density [6]–[10].

Currently, single-phase-shift (SPS) modulation remains the most common method used in the 1ph-DAB and 3ph-DAB converters [1], [8]. This control method applies a simple power transmission control mechanism. Although SPS control limits the soft-switching operation range, it provides the high circulating current and high rms inductor current at the light-load conditions with a large voltage variation ratio. It also causes the converter to operate in the hard-switching mode and dramatically degrades the converter efficiency [11]. To overcome these issues, several novel control strategies have been proposed in the 1ph-DAB, such as extended phase-shift control, dual-phase-shift control, and triple phase-shift (TPS) control. These control methods can extend the zero-voltage switching (ZVS) range and reduce the current's rms value to enhance the efficiency of the DAB converter [1], [12].

Limited studies address the 3ph-DAB converter's poor efficiency under light loads. van Hoek et al. [13] proposed a 1ph-DAB operating mode to control 3ph-DAB by controlling two-phase legs to synchronize operation. Even if adopting triangular and trapezoidal modulation under light-load conditions will reduce the current's rms value, this method is not an optimal scheme and cannot cover the converter's entire power range. Su and Tang [14] controlled the driving signals of dual active bridges to operate at a fixed 1/3 duty cycle on both sides to boost

Manuscript received 4 December 2021; revised 1 April 2022 and 26 May 2022; accepted 8 July 2022. Date of publication 21 July 2022; date of current version 6 September 2022. This work was supported in part by the State Key Laboratory of Electrical Insulation and Power Equipment under Grant EIPE21301 and in part by the National Natural Science Foundation of China under Grant 51907156. Recommended for publication by Associate Editor M. Amirabadi. *(Corresponding author: Jinjun Liu.)*

The authors are with the State Key Laboratory of Electrical Insulation and Power Equipment, School of Electrical Engineering, Xi'an Jiaotong University, Xi'an 710049, China (e-mail: chenhui_xjtu@stu.xjtu.edu.cn; oysd1989@stu.xjtu.edu.cn; jjliu@mail.xjtu.edu.cn; www.981121qq.com@stu.xjtu.edu.cn).

Color versions of one or more figures in this article are available at https://doi.org/10.1109/TPEL.2022.3192781.

Digital Object Identifier 10.1109/TPEL.2022.3192781

the efficiency. However, it cannot enhance the efficiency of the entire power range and its ZVS region is not revealed under this control method. Li et al. [15] and Huang et al. [16] improved the method used in the literature [14] by introducing the variable duty cycle control of the primary and secondary sides to optimize the current's rms value and increase efficiency. However, the duty cycle control makes the current asymmetrical and it cannot realize all switches ZVS turn-ON [17]. Moreover, these methods are extremely complex. This restricts the method's further practical application. Almost all of the aforementioned control methods rely on duty cycle control with symmetrical phase-shift and fail to provide ZVS capability over the entire power range with all power switches.

As aforementioned, almost all proposed methods of 3ph-DAB are employed symmetrical phase-shift angle of 1/3 among three-phase legs. These methods change the duty cycle of three-phase dual active bridges to improve the converter's efficiency. However, the variation of duty cycle will cause the phase current to be asymmetrical in the positive and negative half-cycles. It will bring about the consequence that ZVS turn-ON cannot be realized in both upper and lower power switches, and most methods only obtain the numerical solutions that are difficult for practical application. The 3ph-DAB control with variable phase-shift angles among three-phase legs has so far been overlooked in the existing literature. This article proposes a novel asymmetrical phase-shift (APS) control of 3ph-DAB by adopting variable phase-shift angles instead of fixed 1/3 phase-shift angles to address the aforementioned issues and further reduce the conduction and switching losses. This control method can realize the minimum inductor current's rms value and extend the ZVS operation compared with other proposed control methods. Moreover, the analytical solutions of this proposed method are derived to be convenient for practical applications. Experimental results from a 3ph-DAB hardware prototype validate the excellent performances of the proposed method.

The rest of this article is organized as follows. In Section II, the detailed operation principles of 3ph-DAB are presented. According to the equivalent circuit of 3ph-DAB, the expressions of three-phase voltages, currents, and transmission power can be derived. Based on these principles, the novel APS method is proposed in Section III. In Section III, the switching sequences and multifrequency approximation converter model under the proposed novel APS control are derived in Section III-A to avoid analyzing complex and numerous switching modes. Then, according to the minimum conduction loss principle and ZVS conditions, the optimal strategy acquired using the interior-point method combined with the Lagrange multiplier method is presented in Section III-B. Subsequently, the comparison with the performance of the proposed novel APS method and SPS control is presented in Section III-C. In Section IV, the result of optimal phase-shift angles obtained by adopting a numerical optimization algorithm in the preceding section will be analyzed. The global optimal condition (GOC) equations are also proposed to validate the conclusions that the minimum 3ph-DAB conduction loss mode in the low-level and high-level power range is the 1ph-DAB and SPS control modes, respectively. The closed-form analytic expressions of optimal phase-shift angles are further derived. The effectiveness of the optimal strategy is validated using simulations and experiments, which are presented in Section V. Finally, Section VI concludes this article.

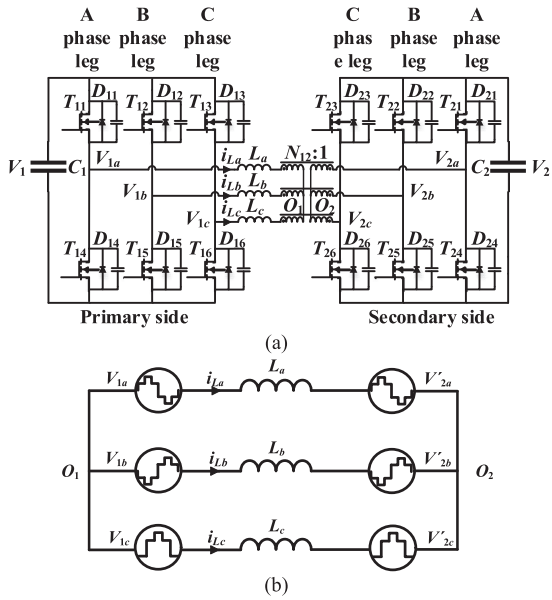

Fig. 1. Topology schematic and equivalent circuit of 3ph-DAB. (a) Topology schematic of 3ph-DAB. (b) equivalent circuit of 3ph-DAB.

II. Operation Principle of 3ph-DAB

Fig. 1(a) shows the 3ph-DAB topology, and its equivalent circuit is shown in Fig. 1(b). Fig. 1(a) shows the circuit schematic of 3ph-DAB converter. V_1 and V_2 represent the input and output dc voltages, respectively. C_1 is the input filter capacitor and C_2 is the output filter capacitor to support dc link voltage. T_{xy} ($x = 1$ and 2; $y = 1$, 2, 3, 4, 5, and 6) are the power switches composed of three-phase active dual bridges in the primary and secondary sides. D_{xy} denotes the corresponding antiparallel diode of power switch. L_a, L_b, and L_c are the equivalent three-phase inductors including transformer leakage inductance and other external inductors. The three-phase high-frequency transformers with Y–Y connection forms the link bridge between the V_1-side (primary side) and V_2-side (secondary side). O_1 and O_2 denote the neutral point of the V_1- and V_2-sides. N_{12} is the turn ratio from V_1-side to V_2-side of the three-phase transformers. v_{1a}, v_{1b}, and v_{1c} are the three-phase voltages in the V_1-side bridge. v_{2a}, v_{2b}, and v_{2c} are the three-phase voltages in the V_2-side bridge. i_{La}, i_{Lb}, and i_{Lc} are the three-phase currents that pass through the arm inductors.

Fig. 1(b) shows the equivalent 3ph-DAB circuit derived from the superposition theorem and Kirchhoff's Laws. v'_{2a}, v'_{2b}, and v'_{2c} are the equivalent phase voltages in the V_1-side that are converted by the V_2-side phase voltages of v_{2a}, v_{2b}, and v_{2c}. Three-phase voltages are symmetrical with 1/3 phase-shift angles in the conventional control method. The three-phase dual active bridge voltages of V_1-side and V_2-side can be regarded

as multilevel alternating current (ac) voltage sources with Y–Y connection. In general, magnetic inductance of transformer in 3ph-DAB converter is extremely large. This implies that the transformer's magnetic inductance is commonly neglected. Thus, the equivalent 3ph-DAB circuit can be presented as the connection between three-phase inductors and equivalent ac voltage sources.

For analysis simplification, switching function $S_{xy}(t)$ ($x = 1$ and 2; $y = a$, b, and c) will be introduced into the three-phase dual active bridges on both sides. $x = 1$ indicates that this power switch is located on the V_1-side, whereas $x = 2$ indicates this power switch is on the V_2-side. Similarly, $y = a$, b, and c imply that this power switch is located on the A, B, and C phase legs, respectively. The value of $S_{xy}(t)$ is equal to 1, which implies that the upper power switch of the corresponding side and phase is ON and the lower power switch is OFF. The reverse is also true. According to the switching function $S_{xy}(t)$, the three-phase voltages can be expressed as follows:

$$\begin{cases} v_{1a}(t) = \dfrac{\mathrm{V}_1(2S_{1a}(t) - S_{1b}(t) - S_{1c}(t))}{3} \\ v_{1b}(t) = \dfrac{\mathrm{V}_1(2S_{1b}(t) - S_{1a}(t) - S_{1c}(t))}{3} \\ v_{1c}(t) = \dfrac{\mathrm{V}_1(2S_{1c}(t) - S_{1b}(t) - S_{1a}(t))}{3} \end{cases} \tag{1}$$

$$\begin{cases} v'_{2a}(t) = \dfrac{\mathrm{N}_{12}\mathrm{V}_2(2S_{1a}(t) - S_{1b}(t) - S_{1c}(t))}{3} \\ v'_{2b}(t) = \dfrac{\mathrm{N}_{12}\mathrm{V}_2(2S_{1b}(t) - S_{1a}(t) - S_{1c}(t))}{3} \\ v'_{2c}(t) = \dfrac{\mathrm{N}_{12}\mathrm{V}_2(2S_{1c}(t) - S_{1b}(t) - S_{1a}(t))}{3}. \end{cases} \tag{2}$$

From the equivalent circuit shown in Fig. 1(b), the phase currents i_{La}, i_{Lb}, and i_{Lc} can also be derived as follows:

$$\begin{cases} i_{La}(t) = i_{La}(0) + \dfrac{1}{L}\int_0^t (v_{1a}(\tau) - v'_{2a}(\tau))d\tau \\ i_{Lb}(t) = i_{Lb}(0) + \dfrac{1}{L}\int_0^t (v_{1b}(\tau) - v'_{2b}(\tau))d\tau \\ i_{Lc}(t) = i_{Lc}(0) + \dfrac{1}{L}\int_0^t (v_{1c}(\tau) - v'_{2c}(\tau))d\tau \end{cases} \tag{3}$$

where τ denotes the time within a period. Furthermore, the rms value of three-phase currents and powers can be described as follows:

$$\begin{cases} I_a = \sqrt{\dfrac{1}{T_s}\int_0^{Ts} i_{La}^2(t)dt} \\ I_b = \sqrt{\dfrac{1}{T_s}\int_0^{Ts} i_{Lb}^2(t)dt} \\ I_c = \sqrt{\dfrac{1}{T_s}\int_0^{Ts} i_{Lc}^2(t)dt} \end{cases} \tag{4}$$

$$\begin{cases} P_a = \dfrac{1}{T_s}\int_0^{T_s} v_{1a}(t)i_{La}(t)dt \\ P_b = \dfrac{1}{T_s}\int_0^{T_s} v_{1b}(t)i_{Lb}(t)dt \\ P_c = \dfrac{1}{T_s}\int_0^{T_s} v_{1c}(t)i_{Lc}(t)dt. \end{cases} \tag{5}$$

For a more general conclusion, the standardization operation will be performed using the current and power expressions. The based value of current and power are shown as follows:

$$\begin{cases} I_b = \dfrac{\mathrm{V}_1 T_s}{2\pi L_s} \\ P_b = \dfrac{\mathrm{V}_1^2 T_s}{2\pi L_s}. \end{cases} \tag{6}$$

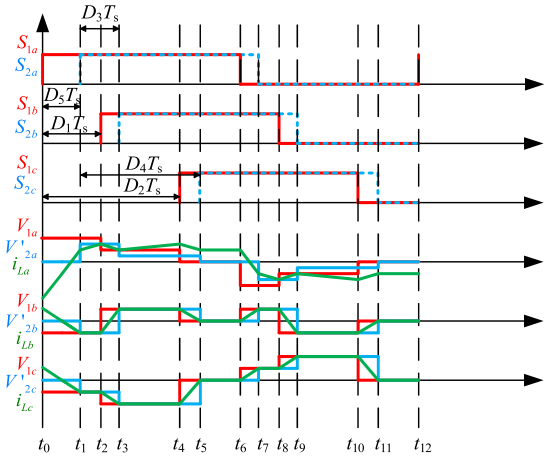

Fig. 2. Switching sequences and the typical three-phase operation waveforms under APS control.

III. APS Control of 3ph-DAB

In this section, a novel control method is proposed to minimize the 3ph-DAB current's rms value by introducing asymmetrical three-phase-shift angles. In this proposed control method, phase A does not lead phase B by $2\pi/3$, nor does it lag C by $2\pi/3$. The phase-shift angles among A, B, and C are flexible with any value. Section III will be divided into three parts: In the first part, a multifrequency approximation model [18] of 3ph-DAB will be built under the proposed APS control scheme to avoid analyzing complex and numerous switching modes. In the second part, to solve the optimal values of five phase-shift angles in the proposed control scheme, the interior-point method combined with the Lagrange multiplier algorithm will be employed to obtain numerical solutions of five phase-shift angles to make 3ph-DAB attain minimum conductance loss and extend the soft-switching range. In the final part, a comprehensive comparison of the proposed APS control scheme and conventional SPS control method will be presented. The comparison results will reveal the significant advantages of the proposed control method.

A. Multifrequency Approximation Model of 3ph-DAB Under APS Control

Fig. 2 illustrates the switching sequences and typical three-phase operation waveforms under APS control. In the APS control scheme, the variable phase-shift angles instead of $2\pi/3$ (or described as $T_s/3$ and T_s are the switching periods) among the three-phase legs are adopted. Power switch pairs of each phase leg operate at complementary mode and duty cycles of all switches, which are maintained at 0.5. Fig. 2 shows that D_1 and D_2 denote the variable phase-shift angles between phases B and A and C and A in V_1-side, respectively, whereas D_3 and

D_4 denote the variable phase-shift angles between phases B and A and C and A in V_2-side, respectively. The phase-shift angle between T_{11} in V_1-side and T_{21} in V_2-side will be defined as D_5 to control the power transfer. The value range of these five phase-shift angles can be described as $0 \le D_1 \le 1$, $0 \le D_2 \le 1$, $0 \le D_3 \le 1$, $0 \le D_4 \le 1$, and $-0.5 \le D_5 \le 0.5$. It is evident that the conventional SPS control is a special APS control mode with $D_1 = 1/3$, $D_2 = 2/3$, $D_3 = 1/3$, and $D_4 = 2/3$ based on the aforementioned analysis.

In the proposed APS control, the adjustable phase-shift angles D_1, D_2, D_3, and D_4 will generate an asymmetrical five-level ac source on both sides. However, the voltage seconds over the entire switching period are always balanced. This ensures that the phase currents flowing into the transformer have no dc bias and will be avoided in the magnetic saturation problem. Under the APS control, the power switch pairs in each phase leg are complementary, and the duty cycles of switches are 0.5. This implies that the three-phase voltages and currents are always odd symmetrical at half switching period (see Fig. 2). According to the switching functions, as aforementioned, the three-phase switching functions on both sides can be illustrated as follows:

$$S_{1a}(t) = \begin{cases} 1, 0 \le t \le \dfrac{T_s}{2} \\ 0, \dfrac{T_s}{2} \le t \le T_s \end{cases}$$

$$S_{1b}(t) = \begin{cases} 1, D_1T_s \le t \le D_1T_s + \dfrac{T_s}{2} \\ 0, D_1T_s + \dfrac{T_s}{2} \le t \le T_s \&\& 0 \le t \le D_1T_s \end{cases}$$

$$S_{1c}(t) = \begin{cases} 1, D_2T_s \le t \le D_2T_s + \dfrac{T_s}{2} \\ 0, D_2T_s + \dfrac{T_s}{2} \le t \le T_s \&\& 0 \le t \le D_2T_s \end{cases} \tag{7a}$$

$$S_{2a}(t) = \begin{cases} 1, D_5T_s \le t \le D_5T_s + \dfrac{T_s}{2} \\ 0, D_5T_s + \dfrac{T_s}{2} \le t \le T_s \&\& 0 \le t \le D_5T_s \end{cases}$$

$$S_{2b}(t) = \begin{cases} 1, D_3T_s + D_5T_s \le t \le D_3T_s + D_5T_s + \dfrac{T_s}{2} \\ 0, D_3T_s + D_5T_s + \dfrac{T_s}{2} \le t \le T_s \&\& 0 \\ \le t \le D_3T_s + D_5T_s \end{cases}$$

$$S_{2c}(t) = \begin{cases} 1, D_4T_s + D_5T_s \le t \le D_4T_s + D_5T + \dfrac{T_s}{2} \\ 0, D_4T_s + D_5T_s + \dfrac{T_s}{2} \le t \le T_s \&\& 0 \\ \le t \le D_4T_s + D_5T_s. \end{cases} \tag{7b}$$

Because five phase-shift angles are adjustable, the switching modes of 3ph-DAB are up to $5! = 120$ and hard to be analyzed all. To address this issue, a multifrequency approximation model of APS control will be built to simplify the complex analysis of switching modes. Adopting the Fourier series to expand the switching functions provides the following expressions:

$$\begin{cases} S_{1a}(t) = \dfrac{1}{2} + \sum_{k=1,3,5\ldots}^{+\infty} \dfrac{2\sin(\mathrm{k}\omega t)}{k\pi} \\ S_{1b}(t) = \dfrac{1}{2} + \sum_{k=1,3,5\ldots}^{+\infty} \dfrac{2\sin(\mathrm{k}\omega t - 2kD_1)}{k\pi} \\ S_{1c}(t) = \dfrac{1}{2} + \sum_{k=1,3,5\ldots}^{+\infty} \dfrac{2\sin(\mathrm{k}\omega t - 2kD_2)}{k\pi} \end{cases} \tag{8}$$

$$\begin{cases} S_{2a}(t) = \dfrac{1}{2} + \sum_{k=1,3,5\ldots}^{+\infty} \dfrac{2\sin(\mathrm{k}\omega t - 2kD_5)}{k\pi} \\ S_{2b}(t) = \dfrac{1}{2} + \sum_{k=1,3,5\ldots}^{+\infty} \dfrac{2\sin(\mathrm{k}\omega t - 2k(D_3 + D_5))}{k\pi} \\ S_{2c}(t) = \dfrac{1}{2} + \sum_{k=1,3,5\ldots}^{+\infty} \dfrac{2\sin(\mathrm{k}\omega t - 2k(D_4 + D_5))}{k\pi}. \end{cases} \tag{9}$$

By substituting (8) and (9) into (1) and (2), the phase voltages v_{1a}, v_{1b}, and v_{1c} of the V_1-side and equivalent voltages v'_{2a}, v'_{2b}, and v'_{2c} from the V_2-side to V_1-side can be expressed as follows:

$$v_{1a}(t) = \sum_{k=1,3,5\ldots}^{+\infty} \frac{2\mathrm{V}_1(2\sin(k\omega t) + \sin(\alpha) + \sin(\beta))}{3k\pi}$$

$$v_{1b}(t) = \sum_{k=1,3,5\ldots}^{+\infty} \frac{2\mathrm{V}_1(-\sin(k\omega t) - 2\sin(\alpha) + \sin(\beta))}{3k\pi}$$

$$v_{1c}(t) = \sum_{k=1,3,5\ldots}^{+\infty} \frac{2\mathrm{V}_1(-\sin(k\omega t) + \sin(\alpha) - 2\sin(\beta))}{3k\pi}$$

$$v'_{2a}(t) = \sum_{k=1,3,5\ldots}^{+\infty} \frac{2d\mathrm{V}_1(-2\sin(\varepsilon) + \sin(\chi) + \sin(\delta))}{3k\pi}$$

$$v'_{2b}(t) = \sum_{k=1,3,5\ldots}^{+\infty} \frac{2d\mathrm{V}_1(\sin(\varepsilon) - 2\sin(\chi) + \sin(\delta))}{3k\pi}$$

$$v'_{2c}(t) = \sum_{k=1,3,5\ldots}^{+\infty} \frac{2d\mathrm{V}_1(\sin(\varepsilon) + \sin(\chi) - 2\sin(\delta))}{3k\pi} \tag{10}$$

where

$$\alpha = 2k\pi D_1 - k\omega t, \beta = 2k\pi D_2 - k\omega t$$

$$\chi = 2k\pi(D_3 + D_5) - k\omega t, \delta = 2k\pi(D_4 + D_5) - k\omega t$$

$$\varepsilon = 2k\pi D_5 - k\omega t, d = \frac{N_{12}\mathrm{V}_2}{\mathrm{V}_1}, \omega_s = \frac{2\pi}{T_s}.$$

Similarly, the three-phase inductor currents can also be expressed by substituting (10) into (3). Assume that L_a, L_b, and L_c are all equal to L_s. This implies that the average current during one switching period is zero because the voltage second is balanced in one switching cycle. The parts of $i_{La}(0)$, $i_{Lb}(0)$, and $i_{Lc}(0)$ can be calculated based on this constraint condition. By substituting these values into (3), the three-phase currents

can be expressed as follows:

$$\begin{aligned} i_{La}(t) &= \sum_{k=1,3,5\ldots}^{+\infty} (\mathrm{A}_a + \mathrm{B}_a) \\ i_{Lb}(t) &= \sum_{k=1,3,5\ldots}^{+\infty} (\mathrm{A}_b + \mathrm{B}_b) \\ i_{Lc}(t) &= \sum_{k=1,3,5\ldots}^{+\infty} (\mathrm{A}_c + \mathrm{B}_c) \end{aligned} \tag{11}$$

where

$$\begin{aligned} \mathrm{A}_a &= \frac{2\mathrm{V}_1(-2\cos(k\omega t) + \cos(\alpha) + \cos(\beta))}{3\pi L_s k^2 \omega} \\ \mathrm{B}_a &= \frac{2d\mathrm{V}_1(2\cos(\varepsilon) - \cos(\chi) - \cos(\delta))}{3\pi L_s k^2 \omega} \\ \mathrm{A}_b &= \frac{2\mathrm{V}_1(\cos(k\omega t) - 2\cos(\alpha) + \cos(\beta))}{3\pi L_s k^2 \omega} \\ \mathrm{B}_b &= \frac{2d\mathrm{V}_1(-\cos(\varepsilon) + 2\cos(\chi) - \cos(\delta))}{3\pi L_s k^2 \omega} \\ \mathrm{A}_c &= \frac{2\mathrm{V}_1(\cos(k\omega t) + \cos(\alpha) - 2\cos(\beta))}{3\pi L_s k^2 \omega} \\ \mathrm{B}_c &= \frac{2d\mathrm{V}_1(-\cos(\varepsilon) - \cos(\chi) + 2\cos(\delta))}{3\pi L_s k^2 \omega}. \end{aligned}$$

From (1) and (2), the expressions of three-phase voltages of V_1-side and V_2-side, namely (10), and three-phase currents, namely (11), have similar patterns of (1) and (2). Then, the united expressions can be written as follows.

According to (12) and (13), the expressions of phase voltages (currents) can be composed of three parts: the response of phases A, B, and C. This indicates that each phase voltage (current) is related to three-phase variables. Referring to the structures of the three-phase variables from (12) and (13), as long as the variable (voltage or current) of phase A is derived, variables of other phases (B and C) can be determined immediately

$$\begin{cases} v_{1a}(t) = \dfrac{2\mathrm{A}_1 - B_1 - C_1}{3} \\ v_{1b}(t) = \dfrac{2\mathrm{B}_1 - A_1 - C_1}{3} \\ v_{1c}(t) = \dfrac{2\mathrm{C}_1 - A_1 - B_1}{3} \\ v'_{2a}(t) = \dfrac{2\mathrm{A}_2 - B_2 - C_2}{3} \\ v'_{2b}(t) = \dfrac{2\mathrm{B}_2 - A_2 - C_2}{3} \\ v'_{2c}(t) = \dfrac{2\mathrm{C}_2 - A_2 - B_2}{3} \end{cases} \tag{12}$$

$$\begin{cases} i_{La}(t) = \dfrac{2\mathrm{A}_L - B_L - C_L}{3} \\ i_{Lb}(t) = \dfrac{2\mathrm{B}_L - A_L - C_L}{3} \\ i_{Lc}(t) = \dfrac{2\mathrm{C}_L - A_L - B_L}{3} \end{cases} \tag{13}$$

where

$$\begin{aligned} A_1 &= \sum_{k=1,3,5\ldots}^{+\infty} \frac{2\mathrm{V}_1 \sin(k\omega t)}{3k\pi}, B_1 = \sum_{k=1,3,5\ldots}^{+\infty} \frac{2\mathrm{V}_1 \sin(-\alpha)}{3k\pi} \\ C_1 &= \sum_{k=1,3,5\ldots}^{+\infty} \frac{2\mathrm{V}_1 \sin(-\beta)}{3k\pi} \\ A_2 &= \sum_{k=1,3,5\ldots}^{+\infty} \frac{2d\mathrm{V}_1 \sin(-\varepsilon)}{3k\pi}, B_2 = \sum_{k=1,3,5\ldots}^{+\infty} 2d\mathrm{V}_1 \sin(-\chi) \\ C_2 &= \sum_{k=1,3,5\ldots}^{+\infty} 2d\mathrm{V}_1 \sin(-\delta) \\ A_L &= \sum_{k=1,3,5\ldots}^{+\infty} \frac{-2\mathrm{V}_1 \cos(k\omega t) + 2d\mathrm{V}_1 \cos(\varepsilon)}{3k^2\pi L_s \omega} \\ B_L &= \sum_{k=1,3,5\ldots}^{+\infty} \frac{-2\mathrm{V}_1 \cos(\alpha) + 2d\mathrm{V}_1 \cos(\chi)}{3k^2\pi L_s \omega} \\ C_L &= \sum_{k=1,3,5\ldots}^{+\infty} \frac{-2\mathrm{V}_1 \cos(\beta) + 2d\mathrm{V}_1 \cos(\delta)}{3k^2\pi L_s \omega}. \end{aligned}$$

After deriving the three-phase voltages and currents, the normalized total power can be derived from (5) and (6)

$$\begin{aligned} P_{\mathrm{APS}} &= P_a + P_b + P_c \\ &= \sum_{k=1,3,5\ldots}^{+\infty} \frac{2d}{3k^3\pi^2} (\sin(2(D_1 - D_5)k\pi) \\ &\quad + \sin(2(D_2 - D_5)k\pi) \\ &\quad - 2\sin(2(D_1 - D_3 - D_5)k\pi) \\ &\quad + \sin(2(D_2 - D_4 - D_5)k\pi) \\ &\quad + \sin(2(D_1 - D_4 - D_5)k\pi) \\ &\quad - 2\sin(2(D_2 - D_4 - D_5)k\pi) + 2\sin(2D_5 k\pi) \\ &\quad - \sin(2(D_3 + D_5)k\pi) - \sin(2(D_4 + D_5)k\pi)). \end{aligned} \tag{14}$$

Similarly, the rms value of three-phase currents under APS control can also be derived. For analysis simplification, $I^2{}_{\mathrm{rms}}$ represents the square of I_{rms} to assist the analysis in this article. The normalized $I^2{}_{\mathrm{rms}}$ equation can be presented as (15) following (4) and (6)

$$\begin{aligned} I^2_{\mathrm{rms}} &= I^2_{a\mathrm{rms}} + I^2_{b\mathrm{rms}} + I^2_{c\mathrm{rms}} \\ &= \sum_{k=1,3,5\ldots}^{+\infty} -\frac{4}{3k^4\pi^2} (-3(1 + d^2) + \cos(D_1 \cdot 2k\pi) \end{aligned}$$

$$
\begin{aligned}
&+\cos((D_1-D_2)\cdot 2k\pi)+\cos(D_2\cdot 2k\pi)\\
&+2d\cos((D_2-D_4-D_5)\cdot 2k\pi)\\
&-d(-d(\cos(D_3\cdot 2k\pi)\\
&+\cos((D_3-D_4)\cdot 2k\pi)+\cos(D_4\cdot 2k\pi))\\
&+\cos((D_1-D_5)\cdot 2k\pi)+\cos((D_2-D_5)\cdot 2k\pi)\\
&-2\cos((D_1-D_3-D_5)\cdot 2k\pi)\\
&+\cos((D_2-D_3-D_5)\cdot 2k\pi)\\
&+\cos((D_1-D_4-D_5)\cdot 2k\pi)-2\cos(D_5\cdot 2k\pi)\\
&+\cos((D_3+D_5)\cdot 2k\pi)+\cos((D_4+D_5)\cdot 2k\pi)).
\end{aligned}
\tag{15}
$$

These aforementioned variables, except $I^2{}_{\rm rms}$, are all odd symmetrical at half switching period because the power switch pairs in one phase leg are complementary and the duty cycle of switches is 0.5. $I^2{}_{\rm rms}$ is the square of $I_{\rm rms}$. Thus, it is even symmetrical at half switching period. For analysis simplification, we only need to analyze the 3ph-DAB operation waveform during the half switching period under APS control.

B. Minimum Conduction Loss Control of 3ph-DAB Under APS Control

In the proposed APS control, five degrees of freedom (D_1, D_2, D_3, D_4, and D_5) can provide numerous combinations to transfer the required power with a certain voltage ratio. In this section, based on APS control, the optimized modulation strategy will be proposed to minimize the conduction and switching losses of 3ph-DAB by adjusting phase-shift angles among the three-phase legs of active dual bridges. The situation that power direction is from V_1 to V_2 side ($P>0$) and voltage ratio less than 1 ($d<1$) will be discussed to simplify the analysis. Other work situations can provide a similar analysis.

Based on the analysis of literature [11], [16], the conduction loss is mainly dependent on the $I^2{}_{\rm rms}$ value of 3ph-DAB; the minimum $I^2{}_{\rm rms}$ value means the minimum conduction loss. In this optimized modulation strategy, we aim to achieve the minimum conduction loss under required transmission power and all switches can realize ZVS turn-ON in the entire power range. Alternatively, $I^2{}_{\rm rms}$ must achieve a minimum value under the constraint conditions of the required transmission power and satisfy ZVS conditions. Therefore, this optimization problem can be illustrated as a single optimization object with nonlinear constraint conditions. Based on the aforementioned analysis, the nonlinear constrained programming model can be described as follows:

$$
\begin{aligned}
&{\rm Min} I^2_{\rm rms}(x)\\
&\text{Subject to:}\\
&P_{\rm APS}(x)-P_o=0, {\rm ZVS}_i(x)<0, R_j(x)\le 0\\
&i=1,2,\ldots\ldots 6, j=1,2,\ldots\ldots 10.
\end{aligned}
\tag{16}
$$

P_o is defined as the required transmission power under the required voltage ratio d. $P_{\rm APS}(x)$ is the equation of the transmission power under APS control given by (14), and $I^2{}_{\rm rms}(x)$ is presented as (15) with $x=(D_1, D_2, D_3, D_4,$ and $D_5)$. $R_j(x)$ represents the value range of the five phase-shift angles, and can be rewritten as follows:

$$
\begin{aligned}
&R_1(x)=-D_1\le 0, R_2(x)=D_1-1\le 0\\
&R_3(x)=-D_2\le 0, R_4(x)=D_2-1\le 0\\
&R_5(x)=-D_3\le 0, R_6(x)=D_3-1\le 0\\
&R_7(x)=-D_4\le 0, R_8(x)=D_4-1\le 0\\
&R_9(x)=-D_5-0.5\le 0, R_{10}(x)=D_5-0.5\le 0.
\end{aligned}
\tag{17}
$$

The final constraint condition is the ZVS range of 3ph-DAB under APS control. The currents of power switches must flow through their antiparallel diodes when corresponding switches are turned ON to ensure ZVS operation. This shows that the direction of phase current at the moment of switch turning ON is determined by ZVS operation. In this proposed optimized modulation scheme, all switches, both V_1-side and V_2-side, are required to achieve ZVS turn-ON to enhance the 3ph-DAB efficiency. ${\rm ZVS}_i(x)$ implies the constraint functions, which cause all switches to realize ZVS operation in the entire power range. Because the phase currents are odd symmetrical functions, all switches have the ZVS capability as long as the upper or lower switches can realize ZVS operation in the entire power range within the half switching cycle. This feature simplifies the analysis and we only need to sufficiently analyze the ZVS condition of six switches. In this proposed optimized modulation strategy, based on the phase current direction, the constraint function $ZVS_i(x)$ can be derived as follows:

$$
\begin{aligned}
&{\rm ZVS}_1(x)=i_{La}(t_1)<0, T_{11}\text{ turns on}\\
&{\rm ZVS}_2(x)=i_{La}(t_2)<0, T_{24}\text{ turns on}\\
&{\rm ZVS}_3(x)=i_{Lb}(t_3)<0, T_{12}\text{ turns on}\\
&{\rm ZVS}_4(x)=i_{Lb}(t_4)<0, T_{25}\text{ turns on}\\
&{\rm ZVS}_5(x)=i_{Lc}(t_5)<0, T_{13}\text{ turns on}\\
&{\rm ZVS}_6(x)=i_{Lc}(t_6)<0, T_{26}\text{ turns on}
\end{aligned}
\tag{18}
$$

where t_1, t_2, t_3, t_4, t_5, and t_6 denote the turn-ON moments of the switches T_{11}, T_{24}, T_{12}, T_{25}, T_{13}, and T_{26}, respectively. According to the definition of five phase-shift angles and switching functions, t_1, t_2, t_3, t_4, t_5, and t_6 can be expressed as follows:

$$
\begin{cases}
t_1=0\\
t_2=D_5\cdot T_s+\frac{T_s}{2}\\
t_3=D_1\cdot T_s\\
t_4=(D_5+D_3)\cdot T_s+\frac{T_s}{2}\\
t_5=D_2\cdot T_s\\
t_6=(D_5+D_4)\cdot T_s+\frac{T_s}{2}.
\end{cases}
\tag{19}
$$

$I^2_{\rm rms}(x)$ is the single optimal object function of the nonlinear constrained programming model, which is described as (16). $P_{\rm APS}$-P_o is the equality constraint, whereas $\rm ZVS_{\it i}(\it x)$ ($i = 1, 2, \ldots,$ and 6) and $R_j(x)$ ($j = 1, 2, \ldots,$ and 10) are the inequality constraints. The analytical solutions are difficult to derive because all functions in the nonlinear constrained programming model are related to the five control parameters (D_1, D_2, D_3, D_4, and D_5). To address this issue, the interior-point scheme and Lagrange multiplier method that are commonly applied in solving nonlinear programming with constraints are introduced to deduce numerical solutions of this optimization model and calculate the numerical values of five control parameters (D_1, D_2, D_3, D_4, and D_5).

The interior-point method is a classic method to solve nonlinear optimization problems [19], [20]. This algorithm has been widely applied in power electronics and power systems to solve optimization problems [21]–[23]. The essential idea of the interior-point algorithm is to build the appropriate penalty function for changing the nonlinear program with general constraints to the nonlinear program with equality constraints. And then, the Lagrange multiplier method can be applied to solve this kind of problem. In the interior-point algorithm, a logarithmic function is usually chosen as a penalty function as follows:

$$C(x) = -r\sum_{1}^{i}\ln(-B_i(x)) \tag{20}$$

where $C(x)$ is the penalty function, $B_i(x)$ is the inequality constraint, including $\rm ZVS_{\it i}(\it x)$ and $R_j(x)$, and r is the penalty factor, which will decrease gradually as the number of iterations increasing and eventually approaches 0. Based on the penalty function $C(x)$, if the constraint function $B_i(x)$ is significantly smaller than 0, the solutions certainly satisfy $\rm ZVS_{\it i}(\it x)$ and $R_j(x)$ inequality constraints, and $C(x)$ will attain an extremely small value. If $B_i(x)$ is less than 0 but close to 0 or large than 0, it implies the solutions are likely to break $\rm ZVS_{\it i}(\it x)$ and $R_j(x)$ inequality constraints and $C(x)$ will attain an extremely high value. Adding this penalty function to the objective function as the new optimal target will ensure that the solutions satisfy ZVS constraints and attain the global minimum $I^2_{\rm rms}$ value. Further, the nonlinear optimization program with general constraints in this article can be simplified to the following optimization program with equality constraints:

$$\begin{aligned}&{\rm Min}F(x) = I^2_{\rm rms}(x) + C(x)\\ &\text{Subject to :}\\ &P_{\rm APS}(x) - P_o = 0.\end{aligned} \tag{21}$$

The Lagrange multiplier method can solve this kind of optimization program perfectly, as shown in the literature [19] and [24]. The Lagrange objection function will be constructed as follows:

$$L(x,\lambda) = F(x) + \lambda(P_{\rm APS}(x) - P_o). \tag{22}$$

When the object function $F(x)$ attains its minimum value, the following equations will be satisfied :

$$\begin{cases}\dfrac{\partial L}{\partial D_1} = \dfrac{\partial F(x)}{\partial D_1} + \dfrac{\partial(\lambda(P_{\rm APS}(x) - P_o))}{\partial D_1} = 0\\ \dfrac{\partial L}{\partial D_2} = \dfrac{\partial F(x)}{\partial D_2} + \dfrac{\partial(\lambda(P_{\rm APS}(x) - P_o))}{\partial D_2} = 0\\ \dfrac{\partial L}{\partial D_3} = \dfrac{\partial F(x)}{\partial D_3} + \dfrac{\partial(\lambda(P_{\rm APS}(x) - P_o))}{\partial D_3} = 0\\ \dfrac{\partial L}{\partial D_4} = \dfrac{\partial F(x)}{\partial D_4} + \dfrac{\partial(\lambda(P_{\rm APS}(x) - P_o))}{\partial D_4} = 0\\ \dfrac{\partial L}{\partial D_5} = \dfrac{\partial F(x)}{\partial D_5} + \dfrac{\partial(\lambda(P_{\rm APS}(x) - P_o))}{\partial D_5} = 0\\ \dfrac{\partial L}{\partial \lambda} = (P_{\rm APS}(x) - P_o) = 0.\end{cases} \tag{23}$$

By solving these equations, the $I^2_{\rm rms}(x)$ value with required transmission power under the required voltage ratio d, the optimal phase-shift angles (D_1, D_2, D_3, D_4, and D_5) can be obtained.

Following the numerical solution of (23), the relationship among D_1, D_2, D_3, D_4, and D_5 with varying transmission power P_o and voltage ratio d is presented in Fig. 3.

C. Comparison and Analysis

From the previous section, five optimal phase-shift angles are determined. Substituting these phase-shift angles into (14) and (15), the $I^2_{\rm rms}$ value under the required transferred power can be obtained by adopting the proposed APS control. Further, the analysis and comparison of the conventional SPS control and proposed APS control can be conducted. Fig. 3 illustrates the five optimal phase-shift angles with transmission power $P_{\rm on}$ and voltage ratio d. Fig 3 shows that the five control parameters (D_1, D_2, D_3, D_4, and D_5) obtained through the optimized modulation scheme, as aforementioned, exhibit some interesting features. D_1 and D_2 and D_3 and D_4 have a similar form at the low-level power range. At the medium-level power conditions, the five phase-shift angles are different and asymmetrical, and they operate at SPS control with $D_1 = 1/3$, $D_2 = 2/3$, $D_3 = 1/3$, and $D_4 = 2/3$ at the high-level power conditions. For more intuitive analysis, Fig. 4 shows the numerical solution of the five phase-shift angles adopting the proposed APS control with $d = 0.6$ conditions. It shows that 3ph-DAB operates as a 1ph-DAB mode with $D_1 = D_2$ and $D_3 = D_4$ at light-load conditions. However, at heavy-load conditions, D_1 and D_3 tend to 1/3, and D_2 and D_4 tend to 2/3 (SPS mode). This reveals that SPS and 1ph-DAB mode control are the special cases of APS control and they can attain minimum $I^2_{\rm rms}$ value at heavy and light-load conditions. Fig. 5 demonstrates the comparison of $I^2_{\rm rms}$ with APS and SPS controls under the entire power and voltage ratio ranges. The blue surface in Fig. 5 represents $I^2_{\rm rms}$ with SPS control, whereas the red surface represents $I^2_{\rm rms}$ with APS control. The APS control can decrease $I^2_{\rm rms}$ significantly at light and medium-load conditions with a large voltage variations ratio. At the heavy-load conditions, the APS control gradually becomes the SPS control. Thus, the $I^2_{\rm rms}$ value will be the same under these two control schemes. For a more intuitive analysis, the $d = 0.6$ conditions are taken as an example, as shown in Fig. 6. The red dotted line represents the $I^2_{\rm rms}$ value

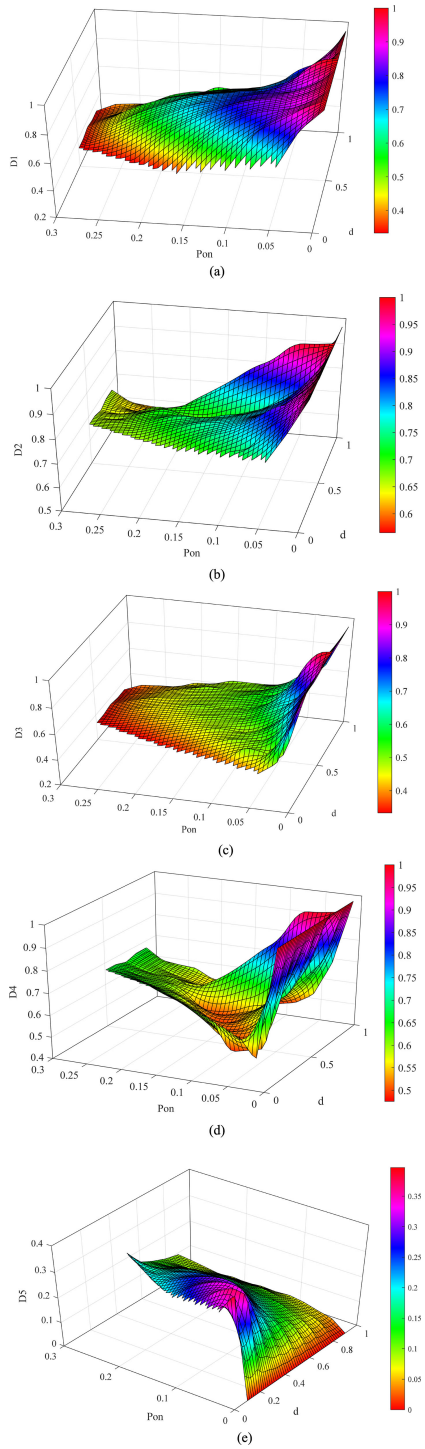

Fig. 3. Optimal phase-shift angles with the required transmission power and voltage ratio. (a) D_1. (b) D_2. (c) D_3. (d) D_4. (e) D_5.

with APS control in the entire power range. The blue dotted line represents the $I^2_{\rm rms}$ value with SPS control in the entire power range. The APS control can achieve a massive reduction in $I^2_{\rm rms}$ in most load ranges. In summary, the proposed APS control of 3ph-DAB can achieve a lower $I^2_{\rm rms}$ value at the most power range. At the light-load conditions, the proposed control scheme makes 3ph-DAB operate like 1ph-DAB to significantly

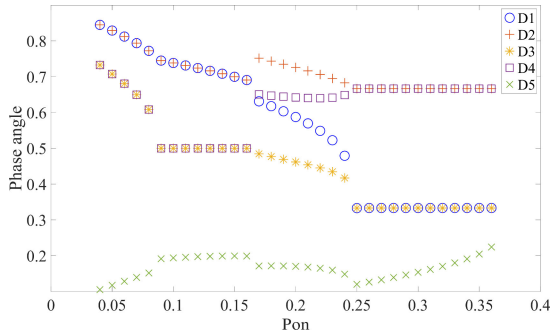

Fig. 4. Optimal phase-shift angles with the required transmission power and voltage ratio $d = 0.6$.

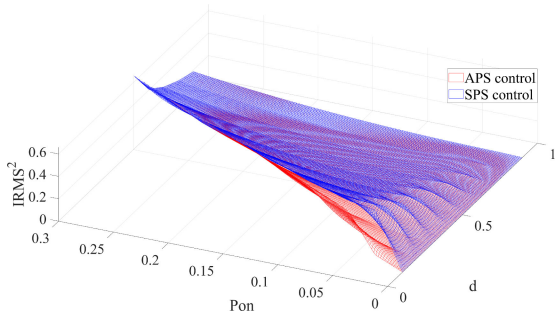

Fig. 5. Comparison of $i^2_{\rm rms}$ value with SPS control and the optimized ASP control with the required transmission power and voltage ratio.

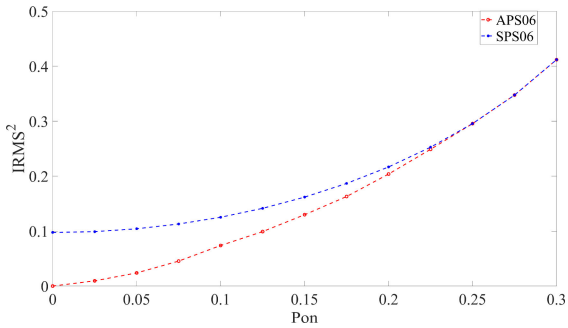

Fig. 6. Comparison of $I^2_{\rm rms}$ value with SPS control and the optimized ASP control with the required transmission power and voltage ratio $d = 0.6$.

reduce the $I^2_{\rm rms}$ value. At the medium-load conditions, the 3ph-DAB adopts the proposed APS control with different and asymmetrical five pahse-shift angles to decrease the $I^2_{\rm rms}$ value. At high-load conditions, the proposed control method gradually converts to the SPS control and achieves the same $I^2_{\rm rms}$ value.

The ZVS capability is also a crucial factor in evaluating the 3ph-DAB control method. This capability can significantly decrease the switching loss. The ZVS region with proposed APS and SPS controls can be determined based on the constraint function (18). Fig. 7 shows a ZVS region comparison of APS and SPS controls. APS control can significantly extend the ZVS turn-ON boundary. Thus, APS control can achieve lower switching loss than SPS control to further improve the 3ph-DAB efficiency.

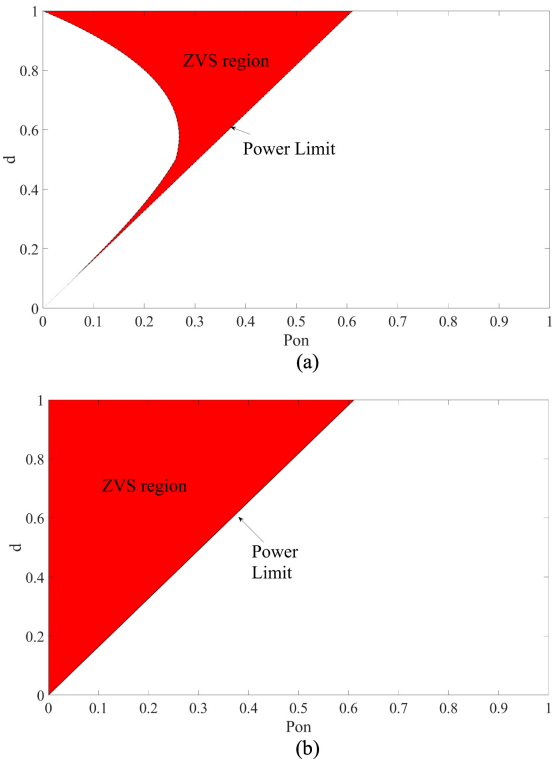

Fig. 7. Comparison of ZVS region with SPS control and the optimized ASP control with the required transmission power and voltage ratio. (a) ZVS region with SPS control. (b) ZVS region with optimized ASP control.

IV. Derivation of Minimum Conduction Loss Control of 3ph-DAB in GOC Equations

Fig. 3 shows that the numerical solutions of the five optimal phase-shift angles with minimum $I^2{}_{\rm rms}$ value have been presented. However, numerical solutions of phase-shift angles are difficult to be used in real-time microcontrollers. Moreover, the numeric solution table is required for the offline calculation in advance. This will increase the difficulty of its practical applications. In addition, the numeric solutions look-up table should be recalculated when the parameters of work conditions are changed. To address these drawbacks, the analytical solutions of the five optimal phase-shift angles will be derived using the GOC equations. These analytical solutions reveal the simple functional relationship among the five phase-shift angles and present interesting conclusions that the optimal mode of 3ph-DAB at low-power level with minimized $I^2{}_{\rm rms}$ value is the 1ph-DAB mode, whereas that at high-power level with minimized $I^2{}_{\rm rms}$ value is the SPS control.

To derive the analytical solutions of the five optimal phase-shift angles with minimum conduction loss under the required transmission power, the GOC equations should be developed. For simplification, the analysis presented in the following is mainly for the condition of voltage ratio $d < 1$ and power direction from the V_1-side to the V_2-side ($P > 0$).

GOC equations are introduced in [25]. First, according to (14) and (15), the total differential of the normalized power and $I^2{}_{\rm rms}$ about phase-shift angles are derived as follows:

$$\begin{cases} \Delta P_{\rm APS} = P_{\rm APS}(G+\Delta d) - P_{\rm APS}(G) \\ \approx \dfrac{dP_{\rm APS}}{dG} = \dfrac{\partial P_{\rm APS}}{\partial D_1}\Delta d_1 + \dfrac{\partial P_{\rm APS}}{\partial D_2}\Delta d_2 + \dfrac{\partial P_{\rm APS}}{\partial D_3}\Delta d_3 \\ + \dfrac{\partial P_{\rm APS}}{\partial D_4}\Delta d_4 + \dfrac{\partial P_{\rm APS}}{\partial D_5}\Delta d_5 \\ \Delta I^2_{\rm rms} = I^2_{\rm rms}(G+\Delta d) - I^2_{\rm rms}(G) \\ \approx \dfrac{dI^2_{\rm rms}}{dG} = \dfrac{\partial I^2_{\rm rms}}{\partial D_1}\Delta d_1 + \dfrac{\partial I^2_{\rm rms}}{\partial D_2}\Delta d_2 \\ + \dfrac{\partial I^2_{\rm rms}}{\partial D_3}\Delta d_3 + \dfrac{\partial I^2_{\rm rms}}{\partial D_4}\Delta d_4 + \dfrac{\partial I^2_{\rm rms}}{\partial D_5}\Delta d_5 \end{cases} \tag{24}$$

where G is the solution vector of phase-shift angles, and $G = (D_1, D_2, D_3, D_4, \text{and } D_5)$.

Further, the evaluation function $\varphi(i)$ has been constructed to evaluate the performance of each phase-shift angle, and $\varphi(i)$ can function as the intermediate variable of the GOC equations to obtain a global optimal result

$$\varphi(i) = \frac{\frac{\partial I^2_{\rm rms}}{\partial D_i}}{\frac{\partial P_{\rm APS}}{\partial D_i}} (i = 1, 2, 3, 4, 5). \tag{25}$$

The evaluation function $\varphi(i)$ is defined as the ratio of the partial derivative of the transmission power $P_{\rm APS}$ to $I^2{}_{\rm rms}$ with each control phase-shift angle $D_{\rm i}$. For the given static-operating point, $G_{\rm static} = (D_{1\rm static}, D_{2\rm static}, D_{3\rm static}, D_{4\rm static}, \text{and } D_{5\rm static})$ with voltage ratio d, we consider the general situation that the evaluation functions $\varphi(i)$ are not equal. Assuming that only the phase-shift angles, $D_{1\rm static}$ and $D_{2\rm static}$, have small perturbations and $0 < \varphi(2) < \varphi(1)$, then the inequation can be described as follows:

$$\varphi(1) = \frac{\frac{\partial I^2_{\rm rms}}{\partial D_1}|_{D_1=D_{1\rm static}}}{\frac{\partial P_{\rm APS}}{\partial D_1}|_{D_1=D_{1\rm static}}} > \varphi(2) = \frac{\frac{\partial I^2_{\rm rms}}{\partial D_2}|_{D_2=D_{2\rm static}}}{\frac{\partial P_{\rm APS}}{\partial D_2}|_{D_2=D_{2\rm static}}} > 0. \tag{26}$$

Formula (26) suggests that the $I^2{}_{\rm rms}$ increment caused by D_1 is larger than D_2 for the given increment of the transmission power $P_{\rm APS}$. In the optimal strategy, we aim to achieve the $I^2{}_{\rm rms}$ minimum value at the given transmission power. Thus, another static point $G_{\rm static1} = (D_{1\rm static} - \Delta d_1, D_{2\rm static} + \Delta d_2, D_{3\rm static}, D_{4\rm static}, \text{and } D_{5\rm static})$ will be constructed to make the $P_{\rm APS}(G_{\rm static}) = P_{\rm APS}(G_{\rm static1})$, where Δd_1 and Δd_2 are the small perturbations of D_1 and D_2, respectively. Based on (24), the $P_{\rm APS}(G_{\rm static1})$ and $I^2{}_{\rm rms}(G_{\rm static1})$ can be derived as follows:

$$\begin{cases} P_{\rm APS}(G_{\rm static1}) \approx P_{\rm APS}(G_{\rm static}) - \frac{\partial P_{\rm APS}}{\partial D_1}\Delta d_1 + \frac{\partial P_{\rm APS}}{\partial D_2}\Delta d_2 \\ I^2_{\rm rms}(G_{\rm static1}) \approx I^2_{\rm rms}(G_{\rm static}) \\ - \frac{\partial I^2_{\rm rms}}{\partial D_1}\Delta d_1 + \frac{\partial I^2_{\rm rms}}{\partial D_2}\Delta d_2. \end{cases} \tag{27}$$

According to $P_{\rm APS}(G_{\rm static}) = P_{\rm APS}(G_{\rm static1})$ and (27), the equation can be obtained as follows.

$$\frac{\partial P_{\rm APS}}{\partial D_3}\Delta d_3 = \frac{\partial P_{\rm APS}}{\partial D_4}\Delta d_4. \tag{28}$$

Further, substituting (28) into (26) and (27), the following crucial conclusions will be deduced:

$$\begin{cases} I^2_{\text{rms}}(G_{\text{static1}}) \approx I^2_{\text{rms}}(G_{\text{static}}) - \frac{\partial I^2_{\text{rms}}}{\partial D_1}\Delta d_1 + \frac{\partial I^2_{\text{rms}}}{\partial D_2}\Delta d_2 \\ \Downarrow \\ \frac{\partial I^2_{\text{rms}}}{\partial D_1}\Delta d_1 > \frac{\partial I^2_{\text{rms}}}{\partial D_2}\Delta d_2 \\ \Downarrow \\ I^2_{\text{rms}}(G_{\text{static1}}) < I^2_{\text{RMS}}(G_{\text{static}}). \end{cases} \tag{29}$$

These inequations present the conclusion that the $I^2{}_{\text{rms}}$ (G_{static1}) is less than the $I^2{}_{\text{rms}}$ (G_{static}) at the same transmission power condition. It suggests that the static-operating point G_{static1} is better than G_{static} and can attain lower conduction loss. The optimal phase-shift angles can be obtained at the $\varphi(1) = \varphi(2)$ conditions when D_1 and D_2 have minimal perturbations by repeating aforementioned process. Similarly, considering the small perturbations of G, the static-operating point, $G_{\text{static2}} = (D_1 + \Delta d_1, D_2 + \Delta d_2, D_3 + \Delta d_3, D_4 + \Delta d_4$, and $D_5 + \Delta d_5) = (D_{1\text{opt}}, D_{2\text{opt}}, D_{3\text{opt}}, D_{4\text{opt}}$, and $D_{5\text{opt}}) = G_{\text{opt}}$, can provide the minimum $I^2{}_{\text{rms}}$ when the following equations are satisfied.

$$\begin{aligned} \varphi(1) &= \frac{\frac{\partial I^2_{\text{rms}}}{\partial D_1}\Big|_{D_1=D_{1\text{opt}}}}{\frac{\partial P_{\text{APS}}}{\partial D_1}\Big|_{D_1=D_{1\text{opt}}}} = \varphi(2) = \frac{\frac{\partial I^2_{\text{rms}}}{\partial D_2}\Big|_{D_2=D_{2\text{opt}}}}{\frac{\partial P_{\text{APS}}}{\partial D_2}\Big|_{D_2=D_{2\text{opt}}}} \\ &= \varphi(3) = \frac{\frac{\partial I^2_{\text{rms}}}{\partial D_3}\Big|_{D_3=D_{3\text{opt}}}}{\frac{\partial P_{\text{APS}}}{\partial D_3}\Big|_{D_3=D_{3\text{opt}}}} = \varphi(4) = \frac{\frac{\partial I^2_{\text{rms}}}{\partial D_4}\Big|_{D_4=D_{4\text{opt}}}}{\frac{\partial P_{\text{APS}}}{\partial D_4}\Big|_{D_4=D_{4\text{opt}}}} \\ &= \varphi(5) = \frac{\frac{\partial I^2_{\text{rms}}}{\partial D_5}\Big|_{D_5=D_{5\text{opt}}}}{\frac{\partial P_{\text{APS}}}{\partial D_5}\Big|_{D_5=D_{5\text{opt}}}}. \end{aligned} \tag{30}$$

Formulae (30) are the GOC equations. By combining (30) with transmission power expression[see (14)], the analytical solutions of these optimal phase-shift angles $G_{\text{opt}} = (D_{1\text{opt}}$, $D_{2\text{opt}}, D_{3\text{opt}}, D_{4\text{opt}}$, and $D_{5\text{opt}})$ can be derived.

B. Solution of GOC Equation in the 3ph-DAB Converter

According to the GOC equations [see (30)], the analytical expressions of optimal phase-shift angles $G_{\text{opt}} = (D_{1\text{opt}}, D_{2\text{opt}}$, $D_{3\text{opt}}, D_{4\text{opt}}$, and $D_{5\text{opt}})$ can be determined by solving (30). In the 3ph-DAB converter, the $\varphi(1)$, $\varphi(2)$, $\varphi(3)$, $\varphi(4)$, and $\varphi(5)$ can be derived as Fourier series as follows:

$$\begin{aligned} &\frac{\frac{\partial I^2_{\text{rms}}(k)}{\partial D_1}}{\frac{\partial P_{\text{APS}}(k)}{\partial D_1}} = \frac{\text{Num}(kD_1)}{\text{Den}(kD_1)}, \frac{\frac{\partial I^2_{\text{rms}}(k)}{\partial D_2}}{\frac{\partial P_{\text{APS}}(k)}{\partial D_2}} = \frac{\text{Num}(kD_2)}{\text{Den}(kD_2)} \\ &\frac{\frac{\partial I^2_{\text{rms}}(k)}{\partial D_3}}{\frac{\partial P_{\text{APS}}(k)}{\partial D_3}} = \frac{\text{Num}(kD_3)}{\text{Den}(kD_3)}, \frac{\frac{\partial I^2_{\text{rms}}(k)}{\partial D_4}}{\frac{\partial P_{\text{APS}}(k)}{\partial D_4}} = \frac{\text{Num}(kD_4)}{\text{Den}(kD_4)} \\ &\frac{\frac{\partial I^2_{\text{rms}}(k)}{\partial D_5}}{\frac{\partial P_{\text{APS}}(k)}{\partial D_5}} = -\frac{\text{Num}(kD_5)}{\text{Den}(kD_5)}. \end{aligned} \tag{31}$$

In (31), the variables of Num(kD_i) and Den(kD_i) ($i = 1$, 2, 3, 4, and 5) are demonstrated in detail as follows:

$$\begin{aligned} \text{Num}(kD_1) = &\sum_{k=1,3,5\ldots}^{+\infty} 2(\sin(A(D_1)) + \sin(B(D_1)) \\ &- d(\sin(C(D_1)) - 2\sin(D(D_1)) + \sin(E(D_1)))) \\ \text{Den}(kD_1) = &\sum_{k=1,3,5\ldots}^{+\infty} dkL_s\omega(\cos(C(D_1)) \\ &- 2\cos(D(D_1)) + \cos(E(D_1))) \end{aligned} \tag{32a}$$

$$\begin{aligned} \text{Num}(kD_2) = &\sum_{k=1,3,5\ldots}^{+\infty} 2(\sin(A(D_2)) - 2\sin(B(D_1)) \\ &- d(\sin(C(D_2)) + \sin(D(D_2)) - 2\sin(E(D_2)))) \\ \text{Den}(kD_2) = &\sum_{k=1,3,5\ldots}^{+\infty} dkL_s\omega(\cos(C(D_2)) \\ &+ 2\cos(D(D_2)) - 2\cos(E(D_2)) \end{aligned} \tag{32b}$$

$$\begin{aligned} \text{Num}(kD_3) = &\sum_{k=1,3,5\ldots}^{+\infty} 2(-d\sin(A(D_3)) - d\sin(B(D_3)) \\ &+ 2\sin(D(D_1)) - \sin(D(D_2)) + \sin(F(D_3))) \\ \text{Den}(kD_3) = &\sum_{k=1,3,5\ldots}^{+\infty} kL_s\omega(-2\cos(D(D_1)) \\ &+ \cos(D(D_2)) + \cos(F(D_3))) \end{aligned} \tag{32c}$$

$$\begin{aligned} \text{Num}(kD_4) = &\sum_{k=1,3,5\ldots}^{+\infty} 2(-d\sin(A(D_4)) + d\sin(B(D_3)) \\ &- \sin(E(D_1)) + 2\sin(E(D_2)) + \sin(F(D_4))) \\ \text{Den}(kD_4) = &\sum_{k=1,3,5\ldots}^{+\infty} kL_s\omega(\cos(E(D_1)) \\ &- 2\cos(E(D_2)) + \cos(F(D_4))) \end{aligned} \tag{32d}$$

$$\begin{aligned} \text{Num}(kD_5) = &\sum_{k=1,3,5\ldots}^{+\infty} -((2(\sin(C(D_1)) + \sin(C(D_2)) \\ &- 2\sin(D(D_1) - A(D_5)) + \sin(D(D_2)) + \sin(E(D_1)) \\ &- 2\sin(E(D_2)) + 2\sin(A(D_5)) \\ &- \sin(F(D_3)) - \sin(F(D_4)))) \end{aligned} \tag{32e}$$

$$\begin{aligned} \text{Den}(kD_5) = &\sum_{k=1,3,5\ldots}^{+\infty} kL_s\omega(\cos(C(D_1)) + \cos(C(D_2)) \\ &- 2\cos(D(D_1)) + \cos(D(D_2)) + \cos(E(D_1)) \\ &- 2\cos(E(D_2)) - 2\cos(A(D_5)) \\ &+ \cos(F(D_3)) + \cos(F(D_4))) \end{aligned} \tag{32f}$$

$$A(D_x) = 2D_x k\pi, B(D_x) = 2(D_x - D_{x+1})k\pi$$
$$C(D_x) = 2(D_x - D_5)k\pi, D(D_x) = 2(D_x - D_3 - D_5)k\pi$$
$$E(D_x) = 2(D_x - D_4 - D_5)k\pi, F(D_x) = 2(D_x + D_5)k\pi. \tag{32g}$$

Obviously, the expression of $\varphi(i)$ is extremely complex, and the GOC equation $\varphi(1) = \varphi(2) = \varphi(3) = \varphi(4) = \varphi(5)$ is difficult to solve. The solution expression of the optimal phase-shift angle $G_{\rm opt}$ = ($D_{1\rm opt}$, $D_{2\rm opt}$, $D_{3\rm opt}$, $D_{4\rm opt}$, and $D_{5\rm opt}$) appears to be difficult to derive. Fortunately, we discover that $\varphi(1)$ and $\varphi(2)$ have similar forms of expressions. Therefore, based on the similar form between $\varphi(1)$ and $\varphi(2)$, one of solutions that makes $\varphi(1) = \varphi(2)$ can be derived as follows:

$$D_1 = D_2, D_3 = D_4 \tag{33}$$

Based on (33), $\varphi(1)$ and $\varphi(2)$ can be rewritten as

$$\varphi(1) = \varphi(2)$$
$$= \frac{2 \cdot (\sin(2D_1 k\pi) - d(\sin(2(D_1 - D_5)k\pi))}{dk(\cos(2(D_1 - D_5)k\pi) - \cos(2(D_1 - D_3 - D_5)k\pi))}$$
$$\frac{+d(\sin(2(D_1 - D_3 - D_5)k\pi)))}{dk(\cos(2(D_1 - D_5)k\pi) - \cos(2(D_1 - D_3 - D_5)k\pi))}. \tag{34}$$

Similarly, $\varphi(3)$ and $\varphi(4)$ have a similar form of expression. If we want to make $\varphi(3)$ equal to $\varphi(4)$, then one of the solutions is the same as (33). Thus, $\varphi(3)$ and $\varphi(4)$ can be rewritten as follows:

$$\varphi(3) = \varphi(4)$$
$$= \frac{2 \cdot (\sin(2(D_1 - D_3 - D_5)k\pi) + \sin(2(D_3 + D_5)k\pi)}{k(-\cos(2(D_1 - D_3 - D_5)k\pi) + \cos(2(D_3 + D_5)k\pi))}$$
$$\frac{-d \cdot \sin(2D_3 k\pi))}{k(-\cos(2(D_1 - D_3 - D_5)k\pi) + \cos(2(D_3 + D_5)k\pi))}. \tag{35}$$

Based on the previous analysis, if we want to satisfy the GOC equation $\varphi(1) = \varphi(2) = \varphi(3) = \varphi(4) = \varphi(5)$, two conditions must be initially satisfied. First, $\varphi(1) = \varphi(2)$ and $\varphi(3) = \varphi(4)$. These conditions require $D_1 = D_2$ and $D_3 = D_4$ based on previous analysis. The second condition is that $\varphi(1) = \varphi(3) = \varphi(5)$. To achieve $\varphi(1) = \varphi(3) = \varphi(5)$, the expressions $\varphi(1) = \varphi(3)$ and $\varphi(1) = \varphi(5)$ must be satisfied at $D_1 = D_2$ and $D_3 = D_4$ conditions, respectively. Interestingly, the 3ph-DAB performance at $D_1 = D_2$ and $D_3 = D_4$ means the phase B voltage is in phase with phase C voltage of the primary and secondary sides. In this situation, the three-phase bridges of both sides work at the H-bridge mode and 3ph-DAB can be regarded as the 1ph-DAB, as shown in Fig. 8.

In this mode, the phase-shift angles D_1 and D_3 can be regarded as inner phase-shift angles of the 1ph-DAB in the primary and secondary bridge, respectively. The phase-shift angle D_5 is the outer phase-shift angle between the primary and secondary sides to control the power flow. Further, GOC equation $\varphi(1) = \varphi(2) = \varphi(3) = \varphi\ (4) = \varphi(5)$ can be satisfied by adjusting the inner phase-shift angles D_1 and D_3 and outer phase-shift angle D_5. Alternatively, the optimal target to minimize the $I^2{}_{\rm rms}$ value of 3ph-DAB under APS control will be altered to minimize the

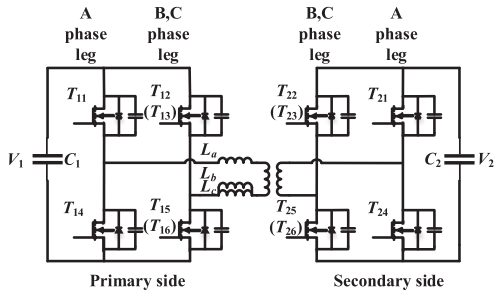

Fig. 8. Schematic diagram of 1ph-DAB mode control.

$I^2{}_{\rm rms}$ value of 1ph-DAB under TPS control. This optimal target can be easily achieved in 1ph-DAB, and several literature [26], [27] have been analyzed in detail. Many well-developed methods can be adopted directly. Thus, a complex optimal target in the 3ph-DAB can be converted to the simple optimal target in the 1ph-DAB. Phase-shift angles expressions can be described in detail as follows:

$$\begin{cases} D_3 = \dfrac{D_1}{d} \\ D_5 = 0 \end{cases}, \text{if } 0 \le \left(D_5 + \frac{D_3 - D_1}{2}\right) \le \frac{1-d}{4}$$

$$\begin{cases} D_3 = 0.5 \\ D_5 = \dfrac{d(-1+D_1) + D_1 + \sqrt{D_1(d^2(-1+D_1) + D_1)}}{2d} \end{cases}$$

$$\text{if } \frac{1-d}{4} \le \left(D_5 + \frac{D_3 - D_1}{2}\right) \le \frac{\sqrt{1-d^2} + d - 1}{4d}$$

$$\begin{cases} D_1 = 0.5 \\ D_3 = 0.5 \end{cases}, \text{if } \frac{\sqrt{1-d^2} + d - 1}{4d} \le \left(D_5 + \frac{D_3 - D_1}{2}\right) \le \frac{1}{4}. \tag{36}$$

The GOC expression $\varphi(1) = \varphi(2) = \varphi(3) = \varphi(4) = \varphi(5)$ will always be met if the phase-shift angle expression is substituted into it. This implies that the aforementioned phase-shift expression is one of solutions of GOC equation. It reveals that the 1ph-DAB converter is the special case of the 3ph-DAB, and the 3ph-DAB's performance at the 1ph-DAB mode can reduce the $I^2{}_{\rm rms}$ value.

Similarly, the other two solutions can be obtained by solving the GOC equation. All solutions can be written in detail as follows:

Solution 1

$$\begin{cases} D_2 = D_1 \\ D_4 = D_3 \\ D_3 = \dfrac{D_1}{d} \\ D_5 = 0 \end{cases}, \text{if } 0 \le \left(D_5 + \frac{D_3 - D_1}{2}\right) \le \frac{1-d}{4}$$

$$\begin{cases} D_2 = D_1 \\ D_4 = D_3 \\ D_3 = 0.5 \\ D_5 = \dfrac{d(-1+D_1)+D_1+\sqrt{D_1(d^2(-1+D_1)+D_1)}}{2d} \end{cases}$$

$$\text{if } \frac{1-d}{4} \le (D_5 + \frac{D_3 - D_1}{2}) \le \frac{\sqrt{1-d^2}+d-1}{4d}$$

$$\begin{cases} D_2 = D_1 \\ D_4 = D_3 \\ D_1 = 0.5 \\ D_3 = 0.5 \end{cases}, \text{if } \frac{\sqrt{1-d^2}+d-1}{4d} \le \left(D_5 + \frac{D_3 - D_1}{2}\right) \le \frac{1}{4}$$

Solution 2

$$\begin{cases} D_1 = \dfrac{1}{3} \\ D_2 = \dfrac{2}{3} \\ D_3 = \dfrac{1}{3} \\ D_4 = \dfrac{2}{3} \end{cases}, \text{if } 0 \le (D_5) \le \frac{1}{4}$$

Solution 3

$$\begin{cases} D_2 = \dfrac{0.177d + 0.394D_1 - 0.750dD_1}{0.221d + 0.439D_1 - D_1} \\ D_4 = \dfrac{0.455(-0.555 - 0.168d + 0.331D_1 + dD_1)}{-0.311 - 0.262d + dD_1} \\ D_3 = \dfrac{0.559 - 0.820d + 1.591D_1 - 0.529dD_1}{2.447 - 1.553d + 2.330D_1 - dD_1} \\ D_5 = \dfrac{0.393 - 1.650D_1 + d(-0.647 + 2.229D_1)}{-0.847 - 1.562D_1 + d(0.608 + D_1)}. \end{cases} \quad (37)$$

All three solutions can satisfy the GOC equation. These solutions reveal three operation modes of 3ph-DAB. The phase-shift angles D_1 and D_3 between B and A and C and A phase legs of primary side are the same as the phase-shift angles D_2 and D_4 between B and A and C and A phase legs of secondary side, respectively, under the condition of solution 1. 3ph-DAB can be regarded as the 1ph-DAB. This operating mode is known as a 1ph-DAB mode. Phase-shift angles among three-phase legs are maintained at 120°, and the transmission power is controlled by the outer phase-shift angle between the primary and secondary bridges under the condition of solution 2. This operating mode is known as SPS mode. Phase-shift angles among three-phase legs are flexible with any value under the condition of solution 3. This operating mode is the general mode of the proposed APS control, which is mentioned in Section III. The 1ph-DAB and SPS modes are the special cases of the APS mode. The transmission power and $I^2{}_{\rm rms}$ value can be derived by putting these solutions into (14) and (15). The relationship between power and $I^2{}_{\rm rms}$ value of three operation modes can be shown as follows:

Mode 1 :

$$\begin{cases} I^2_{\rm rms} = \frac{2\cdot\sqrt{1-d}\cdot P^{\frac{3}{2}}\cdot\sqrt{\frac{\pi}{3}}}{d}, P \in [0, \frac{(d^2-d^3)\pi}{3}] \\ I^2_{\rm rms} = I_{\rm middle}, P \in \left[\frac{(d^2-d^3)\pi}{3}, \frac{(-1+d\cdot(\sqrt{-1+\frac{1}{d^2}}+d))\pi}{3d}\right] \\ I^2_{\rm rms} = \frac{d\pi^2+d^3\pi^2-6P\sqrt{\pi\cdot\sqrt{d(-6P+d\pi)}}}{18d} \\ \frac{-2d\pi^{\frac{3}{2}}\sqrt{d(-6P+d\pi)}}{18d}, P \in \left[\frac{(-1+d\cdot(\sqrt{-1+\frac{1}{d^2}}+d))\pi}{3d}, \frac{d\cdot\pi}{6}\right] \end{cases}$$

Mode 2 :

$$\begin{cases} I^2_{\rm rms} = \frac{d(5+d(6+5d))\pi^2-8\sqrt{2}d\pi^{\frac{3}{2}}\sqrt{d(-9P+2d\pi)}}{81d} \\ \frac{-18P\sqrt{2\pi}\sqrt{d(-9P+2d\pi)}}{81d}, P \in [0, \frac{d\pi}{6}] \\ I^2_{\rm rms} = \frac{\sqrt{\pi}(10(1+d^2)\pi^{\frac{3}{2}}-\frac{18P\sqrt{d(-36P+7d\pi)}}{d}}{162} \\ \frac{-7\pi\sqrt{d(-36P+7d\pi))}}{162}, P \in \left[\frac{d\pi}{6}, \frac{7d\pi}{36}\right] \end{cases}$$

Mode 3 :

$$I^2_{\rm rms} = (-11.3496+P)\left(\frac{1+296.3668d-668.2346P}{160.5906+8176.8538d-9138.8730P} - \frac{1}{(5.4332+P)^2}\right), P \in \left[0, \frac{7d\pi}{36}\right]. \quad (38)$$

In (38), $I_{\rm middle}$ has a complex form and it will be derived detailedly in the Appendix.

Fig. 9(a) shows the comparison of the $I^2{}_{\rm rms}$ value under these three operation modes in the required transmission power and voltage ratio d. For more intuitive analysis, the $d = 0.6$ condition is taken as an example [see Fig. 9(b)]. Fig. 9 shows that APS01 and APS0601 represent mode 1 control of the required power with varying voltage ratios d and a certain voltage ratio $d = 0.6$, respectively. APS02 and APS0602 represent mode 2 control of the required power with varying voltage ratio d and a certain voltage ratio $d = 0.6$, respectively. APS03 and APS0603 represent mode 3 control of required power with varying voltage ratio d and certain voltage ratio $d = 0.6$, respectively. Fig. 9(a) and (b) shows that the optimal transition sequences of operation modes can be determined to minimize the $I^2{}_{\rm rms}$ value, and the following conclusions can also be drawn:

1) 3ph-DAB operating in the 1ph-DAB mode (mode 1 control) can attain the minimum $I^2{}_{\rm rms}$ value under the low-level transmission power condition.

2) Conventional SPS control of 3ph-DAB (mode 2 control) can achieve the minimum $I^2{}_{\rm rms}$ value under the high-level transmission power condition.

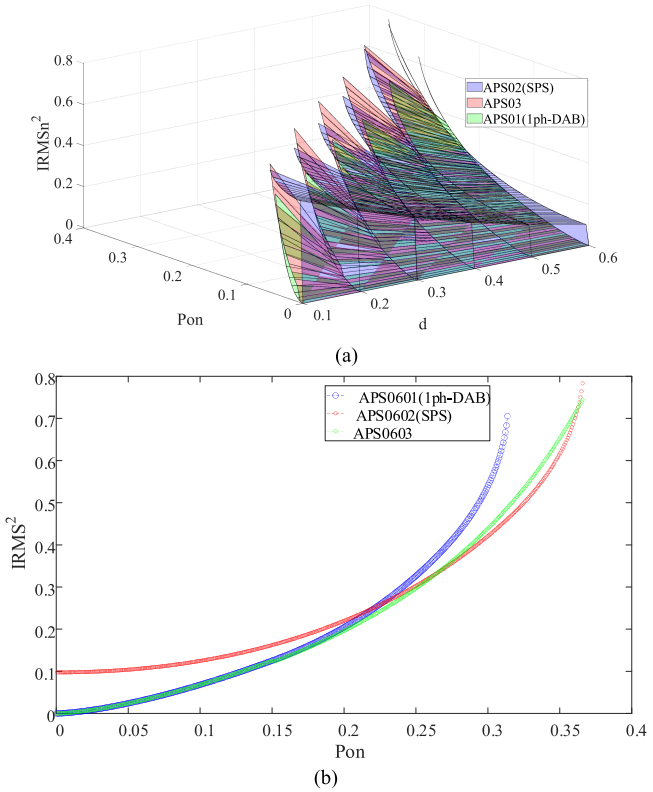

Fig. 9. Comparison of $I^2_{\rm rms}$ value with three mode controls. (a) $I^2_{\rm rms}$ value with three mode controls at the required transmission power and varying voltage ratio conditions. (b) $I^2_{\rm rms}$ value with three mode controls at the required transmission power and voltage ratio $d = 0.6$ conditions.

3) Operation mode 3 of 3ph-DAB can obtain the minimum $I^2_{\rm rms}$ value under the middle-level transmission power condition.

This implies that APS angles can be introduced in the three-phase bridges to achieve optimal control in the middle-level transmission power condition. Obviously, the 1ph-DAB and SPS modes are special cases of the APS mode. Thus, the APS mode can be regarded as the unified control strategy to minimize the $I^2_{\rm rms}$ value. The 1-ph DAB mode will be used as a special case of the APS mode under light-load conditions. The SPS mode will be selected as another special case of the APS mode under heavy-load conditions. The general mode APS control with different phase-shift angles among the three-phase legs is used as the optimal scheme under the medium-load conditions. Based on the aforementioned control strategy, the $I^2_{\rm rms}$ value of 3ph-DAB will be significantly reduced and the efficiency of 3ph-DAB will dramatically improve. These conclusions also verify the numerical solution results that are obtained from the interior-point scheme with the Lagrange multiplier method in Section III.

ZVS capability is also a critical factor in evaluating the control method of 3ph-DAB. The ZVS capability will be determined by substituting the five-phase-shift angles of the optimal APS control strategy into the ZVS constraint function (18). It is gratifying that ZVS capability can be satisfied under the entire power range by adopting the optimal APS control strategy. The results are coincident with the numerical solution results.

TABLE I
EXPERIMENTAL PARAMETER OF 3ph-DAB PROTOTYPE

Description	Variable	Value
Primary DC side voltage	V_1	200V
Secondary DC side voltage	V_2	120V
Series inductor	L_s	20μH
Transformer ratio	N_{12}	1:1
Switching frequency	f_s	50kHz

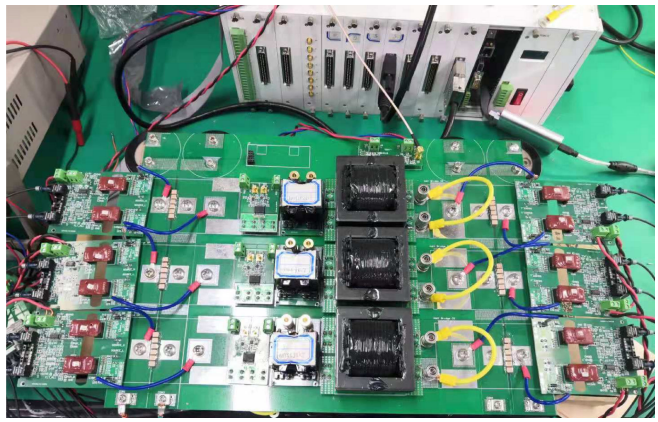

Fig. 10. 3ph-DAB laboratory prototype.

V. EXPERIMENT RESULTS

Experimental results will be presented in this section to verify the proposed method's performance. Table I tabulates the specifications and experimental parameters of the scaled-down laboratory prototype. In this 3ph-DAB laboratory platform, the turns ratio of the primary to the secondary side of the transformer is 1:1, and the voltage ratio of the secondary to the primary side voltage is 0.6. The switching frequency f_s is 50 kHz. The three-phase series inductor value is 20 μH. The electronic power load IT8906A, which is produced by ITECH company, is used as a power load. Fig. 10 shows the photograph of the laboratory prototype. We define that the modes 1–2 of APS control can attain the minimum $I^2_{\rm rms}$ value under light load, medium load, and heavy load, respectively. The power boundary range of light load, medium load, and heavy load can be calculated according to (37), (38), and Fig. 9. In this experimental conditions, the power ranges of light load, medium load, and heavy load can be calculated as $0 < P_{\rm on} < 0.165$, $0.165 < P_{\rm on} < 0.24$, and $P_{\rm on} > 0.24$, respectively.

A. Experimental Results At Low-Level Power Conditions

1) Comparison of $I^2_{\rm rms}$ Value With APS Control and SPS Control: Fig. 11 shows the operating waveforms of 3ph-DAB at the low-level power conditions by adopting the SPS control and optimal strategy proposed in this article, respectively. In this test condition, the dc voltage of the primary side V_1 is maintained at 200 V, whereas the dc voltage of the secondary side V_2 is maintained at 120 V. The transformer ratio is 1:1.

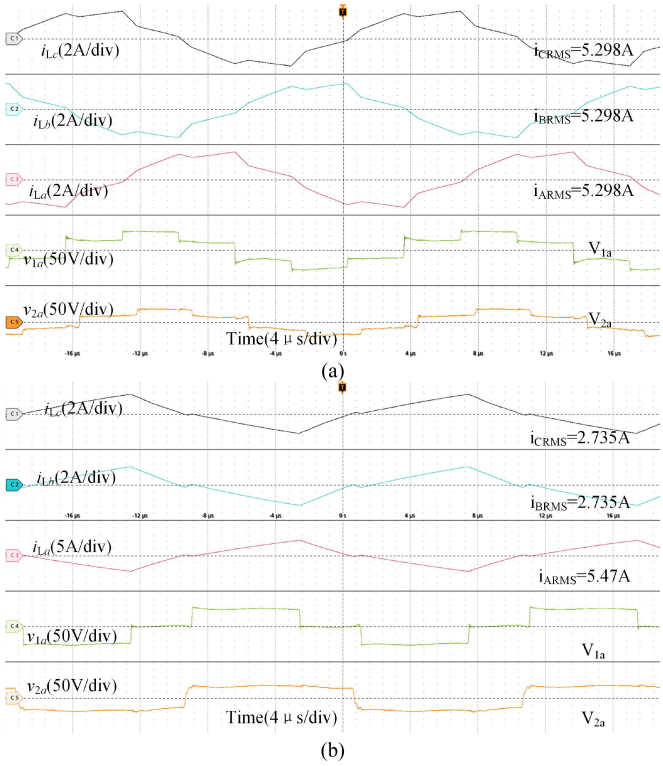

Fig. 11. Operation waveform of 3ph-DAB at low level power conditions. (a) SPS control. (b) Proposed optimized ASP control.

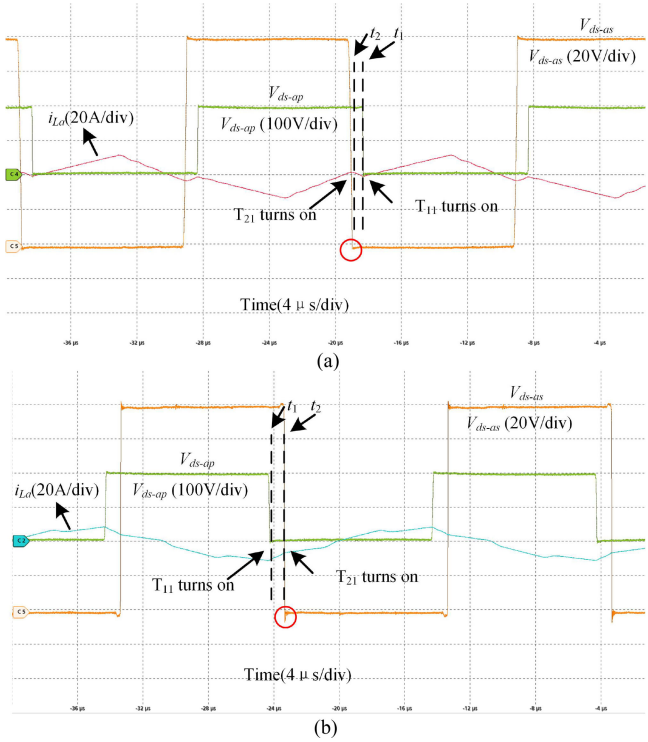

Fig. 12. Turn-ON switching transitions of T_{11} and T_{21} at low power level conditions. (a) Switching waveform of T_{11} and T_{21} with proposed APS control. (b) Switching waveform of T_{11} and T_{21} with SPS control.

The transmission power is 636.6 W, and its normalized value is $0 < P_{\text{on}} = 0.1 < 0.165$. According to the previous analysis, the 3ph-DAB works under the light-load range, and mode 1 of APS modulation is the optimal control, which will attain the minimum $I^2{}_{\text{rms}}$ value among three modes control of APS modulation under the light-load power range. Fig. 11 shows that the green line represents phase A voltage of the primary bridge, the orange line represents the phase A voltage of the secondary bridge, and the red, blue, and dark lines represent the phase A, B, and C currents, respectively. Fig. 11(a) demonstrates the 3ph-DAB waveforms under the SPS control. Fig. 11(b) demonstrates the 3ph-DAB waveforms under the proposed APS control strategy. Fig. 11(b) shows that the optimal control of 3ph-DAB in the low-power level conditions is the 1ph-DAB mode. By comparing the SPS control and the proposed optimal APS control strategy, it is clearly illustrated that the $I^2{}_{\text{rms}}$ value decreases from 84.21 A^2 with the SPS control to 44.88 A^2 with the optimal control strategy in this article. This implies that the massive reduction in $I^2{}_{\text{rms}}$ value is achieved by adopting the optimal control strategy and the efficiency of 3ph DAB is boosted significantly at the low-level power conditions. Interestingly, the triangle shape current is achieved by employing the 3ph-DAB converter's optimal strategy. This current waveform pattern has also been achieved with the 1ph-DAB optimal TPS control in several existing literature. This implies that the optimal control of 1ph-DAB and 3ph-DAB is the same control at the low-power conditions.

2) ZVS Analysis With APS Control and SPS Control: The ZVS analysis will be discussed combined with the experimental

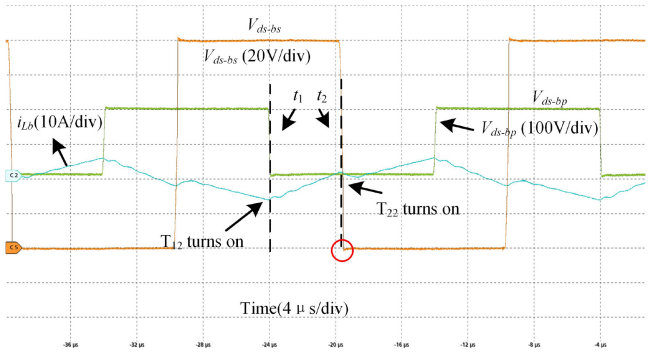

Fig. 13. Turn-ON switching transitions of T_{12} and T_{22} with proposed APS control.

results of proposed APS control and conventional SPS control at the low-level power conditions.

Because the phase current of APS control and conventional SPS control is odd symmetrical at half switching cycle [$i_{La}(t) = -\, i_{La}(t+T_{hs})$, T_{hs} represents half switching period], as long as all top switches of each phase can realize ZVS capability, all switches will achieve ZVS turn-ON. It also implies that the soft-switching characteristics of the top and bottom switches are consistent. Based on previous principle, the ZVS turn-ON analysis will be discussed about switches of phase A in the 3ph-DAB with both proposed APS control and SPS control.

Fig. 12 shows the switching transitions of T_{11} (top switch of the phase A leg in primary side) and T_{21} (top switch of phase

A leg in secondary side) with proposed APS control and conventional SPS control, where the $V_{\mathrm{ds\text{-}ap}}$ and $V_{\mathrm{ds\text{-}as}}$ denote the drain source voltages of T_{11} and T_{21}, respectively. i_{La} represents the phase A current. t_1 and t_2 denote the turn-ON moment of T_{11} and T_{21}. As shown in Fig. 12, the primary switches can realize ZVS turn-ON with both the proposed APS control and conventional SPS control because the $i_{La}(t_1)$ is always less than 0. However, $i_{La}(t_2)$ changes to the large negative value with SPS control. it will make secondary side switch T_{21} operate in hard switching mode and bring the serious voltage overshoot, which is demonstrated in Fig. 12(b). As for APS control, Fig. 12(a) shows that proposed APS modulation can make T_{11} and T_{21} realize ZVS turn-ON. It means that phase A switches of both sides (primary and secondary sides) have the ZVS capability.

Because of the symmetrical control of SPS modulation, the switching waveforms of other phases are similar. It implies that secondary side switches cannot realize ZVS turn-ON at the low-level power conditions for $d < 1$ with conventional SPS control.

As for APS control, Fig. 12 illustrates the ZVS turn-ON phenomenon of phase A switches in both primary and secondary sides with proposed APS modulation. Since the mode 1 of APS control is adopted in the low power level conditions, the operation waveform of phase B is the same as the phase C. It also implies that the soft-switching characteristics of phases B and C are consistent. Take the switching transition of phase B as an example. The transition waveforms are shown as Fig. 13.

As the Fig. 13 shown, since the $i_{Lb}(t_1) < 0$ and $i_{Lb}(t_2) > 0$, switches of phase B in both primary and secondary sides of 3ph-DAB with APS control can realize ZVS turn-ON. Because the soft-switching characteristics of phases B and C are consistent, all switches of 3ph-DAB with APS control can realize the ZVS turn-ON.

B. Experimental Results At Medium-Level Power Conditions

1) Comparison of I^2_{rms} Value With APS Control and SPS Control: Fig. 14 shows the operating waveforms of 3ph-DAB at the middle-level power conditions by adopting the SPS control and optimal strategy proposed in this article, respectively. In this test condition, the dc voltage of the primary side V_1 is maintained at 200 V, whereas the dc voltage of the secondary side V_2 is maintained at 120 V. The transformer ratio is 1:1. The transmission power is 1082.25 W, and its normalized value is $0.165 < P_{\mathrm{on}} = 0.17 < 0.24$. According to the previous analysis, the 3ph-DAB works under the medium-load range, and mode 3 of APS modulation is the optimal control, which will attain the minimum I^2_{rms} value among three modes control of APS modulation under the medium-load power range. Fig. 14(a) demonstrates the 3ph-DAB waveforms under the SPS control, whereas Fig. 14(b) demonstrates the 3ph-DAB waveforms in the proposed APS control strategy under the medium-level power conditions. Fig. 14(b) shows that the phase-shift angles among the three-phase legs are asymmetrical and different in this test condition. By comparing the results of the SPS control and the proposed optimal APS control strategy, it is clearly illustrated that the I^2_{rms} value decreases from $173.51\mathrm{A}^2$ with the SPS control to $138.91\mathrm{A}^2$ with the optimal control strategy in this

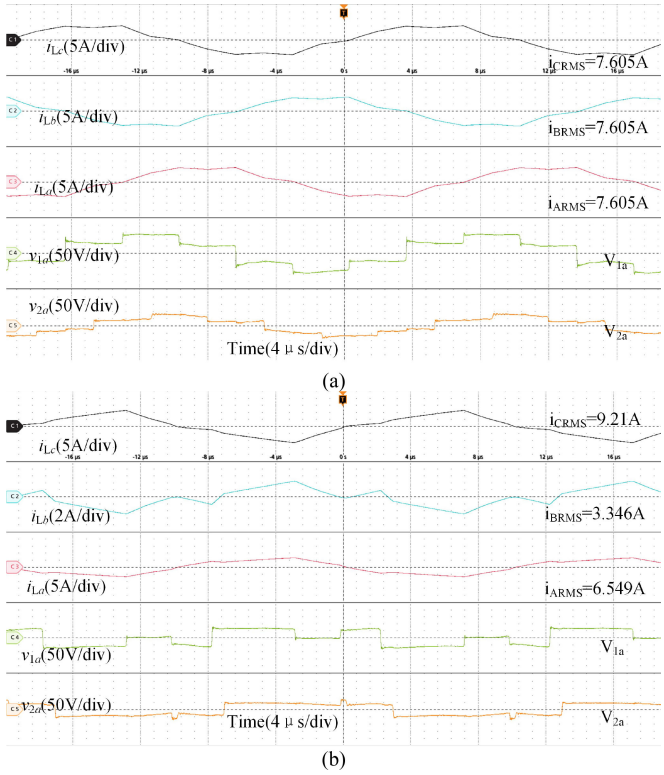

Fig. 14. Operation waveform of 3ph-DAB at medium-level power conditions. (a) SPS control. (b) Proposed optimized ASP control.

article. This implies that the massive I^2_{rms} value reduction is achieved by adopting the optimal control strategy and the 3ph-DAB efficiency is significantly improved at the medium-level power conditions.

2) ZVS Analysis With APS Control and SPS Control: The ZVS analysis will be discussed combined with the experimental results of proposed APS control and conventional SPS control at the medium level power conditions.

Because the phase current of APS control and conventional SPS control is odd symmetrical at half switching cycle [$i_{La}(t) = -i_{La}(t+T_{hs})$, where $\mathrm{T_{hs}}$ represents half switching period], as long as all top switches of each phase can realize ZVS capability, all switches will achieve ZVS turn-ON. It also implies that the soft-switching characteristics of the top and bottom switches are consistent. Based on the abovementioned principle, the ZVS turn-ON analysis will be discussed about switches of phase B in the 3ph-DAB with both the proposed APS control and SPS control.

Fig. 15 shows the switching transitions of T_{12} (top switch of the phase B leg in primary side) and T_{22} (top switch of phase B leg in secondary side) with proposed APS control and conventional SPS control, where the $V_{\mathrm{ds\text{-}bp}}$ and $V_{\mathrm{ds\text{-}bs}}$ denote the drain source voltages of T_{12} and T_{22}, respectively. i_{Lb} represents the phase B current. t_1 and t_2 denote the turn-ON moment of T_{12} and T_{22}. As shown in Fig. 15, the primary switches can realize ZVS turn-ON with both proposed APS control and conventional SPS control because the $i_{Lb}(t_1)$ is always less than 0. However, $i_{Lb}(t_2)$ tends to have the large negative value with SPS control. It will

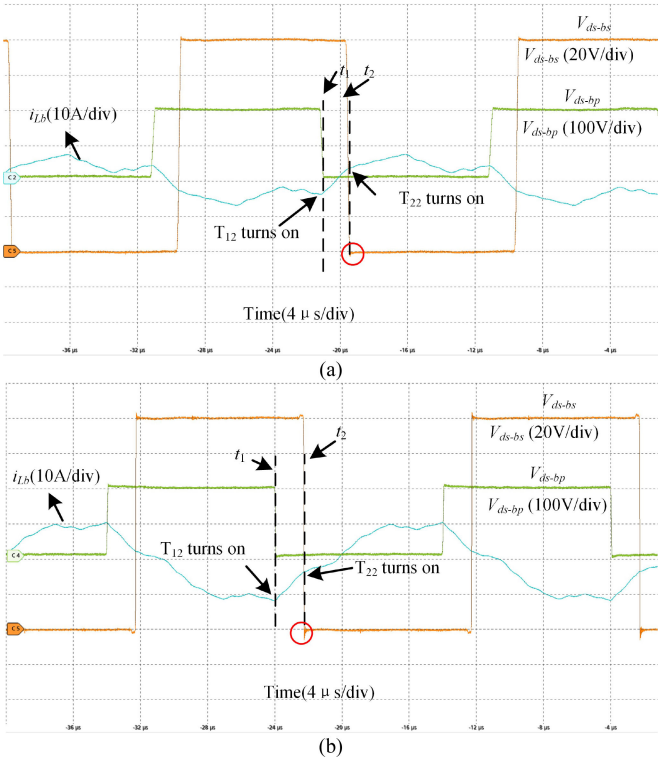

Fig. 15. Turn-ON switching transitions of T_{12} and T_{22} at medium power level conditions.(a) Switching waveform of T_{12} and T_{22} with proposed APS control. (b) Switching waveform of T_{12} and T_{22} with SPS control.

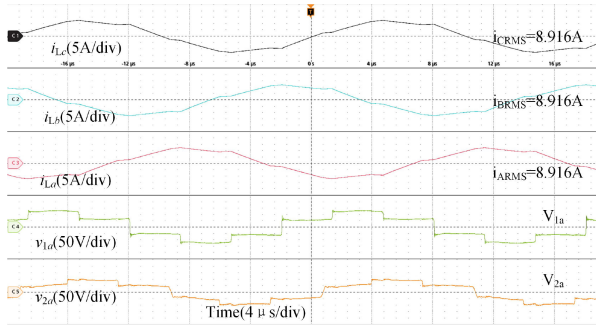

Fig. 16. Operation waveform of 3ph-DAB at high-level power conditions.

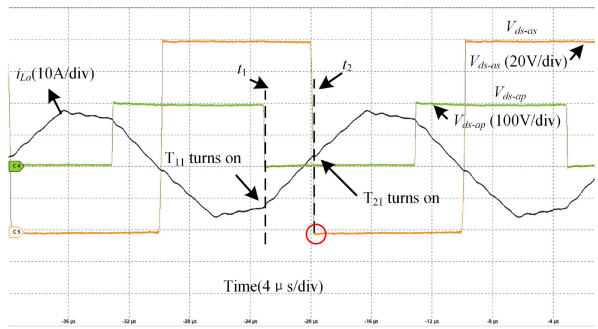

Fig. 17. Turn-ON switching transitions of T_{11} and T_{21} at high power level conditions.

make secondary side switch T_{22} operate in hard switching mode and bring the serious voltage overshoot, which is demonstrated in the Fig. 15(b). As for APS control, Fig. 15(a) shows that the proposed APS modulation can make T_{12} and T_{22} realize ZVS turn-ON. It means that phase B switches of both sides (primary and secondary sides) have the ZVS capability.

Because of the symmetrical control of SPS modulation, the switching waveforms of other phases are similar. It implies that secondary side switches cannot realize ZVS turn-ON at the medium-level power conditions for $d < 1$ with conventional SPS control.

As for APS control, other phases switching conditions are similar as B phase. It concludes that all switches of 3ph-DAB can obtain ZVS turn-ON by adopting the proposed APS modulation.

C. Experimental Results At High-Level Power Conditions

1) Comparison of I^2_{rms} Value With APS Control and SPS Control: Fig. 16 shows the operating waveform of 3ph-DAB at the high-level power conditions by adopting the optimal strategy proposed in this article. In this test condition, the dc voltage of the primary side V_1 is maintained at 200 V, whereas the dc voltage of the secondary side V_2 is maintained at 120 V. The transformer ratio is 1:1. The transmission power is 1655.21W, and its normalized value is $0.24 < P_{\text{on}} = 0.26$. According to the previous analysis, the 3ph-DAB works under the heavy-load range, and mode 2 of APS modulation called as SPS control is the optimal control which will attain the minimum I^2_{rms} value among three modes control of APS modulation under the heavy-load power range. It implies that the proposed optimal APS control strategy tends to be the conventional SPS control scheme under high-power conditions. SPS control becomes the optimal control at high-power conditions to achieve the lowest I^2_{rms} value.

2) ZVS Analysis of SPS Control: At the high-power conditions, APS control changes to the conventional SPS control. The ZVS analysis will be discussed combined with the experimental results. Because of the symmetrical control of SPS modulation, each phase of 3ph-DAB has the same switching characteristics. The switching characteristics of phase A with SPS control is presented as follows.

Fig. 17 shows the switching transitions of T_{11} (top switch of the phase A leg in primary side) and T_{21} (top switch of phase A leg in secondary side) with SPS control at high power level conditions, since $i_{La}(t_1)$ is always less than 0 and $i_{La}(t_2)$ is always larger than 0. SPS control can make all switches of phase A legs in both sides realize ZVS turn-ON. Moreover, because each phase of 3ph-DAB has the same switching characteristics. All switches of 3ph-DAB can achieve ZVS turn-ON by adopting SPS control scheme at high power level conditions.

D. Efficiency of 3ph-DAB With APS Control and Other Modulation Method

Fig. 18 shows the measured efficiency in full-power range of 3ph-DAB laboratory prototype with proposed APS control and other modulation schemes, such as conventional SPS method and ADCC duty cycle control method, which is proposed in [28]. The specific parameters of converter are listed in the Table I. The

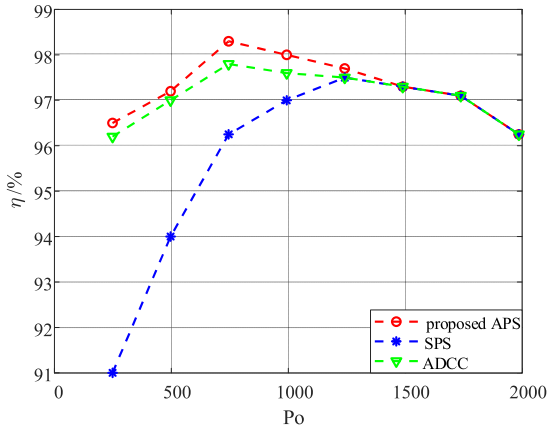

Fig. 18. Comparison of efficiency of 3ph-DAB with APS, SPS, and ADCC control at experimental conditions with $d = 0.6$.

primary dc-side voltage V_1 is 200 V, and the secondary dc-side voltage V_2 maintains 120 V.

As shown in Fig. 18, the P_o represents the transmission power, and the red line, green line and blue line denote the efficiency of 3ph-DAB with APS control, ADCC duty cycle control, and SPS control. It can be concluded that the proposed APS control scheme can present the highest efficiency in the most power range. At the high-power conditions, because the proposed APS modulation and ADCC duty cycle control in [28] evolve into conventional SPS control scheme, the efficiency of these three controls are the same. At the light-load conditions, the efficiency is improved significantly with APS control by comparing with SPS control. ADCC duty cycle method has a slightly lower efficiency compared with the APS control. However, its efficiency improved significantly by comparing with conventional SPS control. In summary, compared with the SPS and ADCC modulation scheme, proposed APS modulation strategy can realize the higher efficiency in the full power range.

E. Comparison of Loss Breakdown With Proposed APS Method and Other Advanced Modulation Method

The total power losses of 3ph-DAB are mainly considering the semiconductor losses and transformer losses. The semiconductors losses can be divided into conduction losses and switching losses of semiconductors. The transformer losses can be divided into winding losses and core losses.

The conduction losses of semiconductors can be calculated by [29], eq. 8, and it is rewritten as follows:

$$P_C = \frac{1}{T_s}\int_0^{T_s} p_c(t)dt = \frac{1}{T_s}\int_0^{T_s} (R_{\text{DSon}} \cdot I_D^2(t))dt = R_{\text{DSon}} \cdot I_{\text{Drms}}^2 \tag{39}$$

where I_{Drms} is the rms value of the drain current, and R_{DSon} is the ON-state resistor and it can be read from the MOSFET datasheet.

The switching losses of semiconductors can be calculated by [29], eq. 6, and it is rewritten as follows:

$$P_s = f_s \cdot (0.5 \cdot \sigma_1 \cdot V_{\text{DS}} \cdot I_{Don} \cdot t_r + 0.5 \cdot \sigma_2 \cdot V_{\text{DS}} \cdot I_{Doff} \cdot t_f + 0.5 \cdot C_{\text{oss}} \cdot V_{\text{DS}}^2 + Q_g \cdot V_g + \sigma_3 \cdot Q_{\text{rr}} \cdot V_{\text{rr}})$$

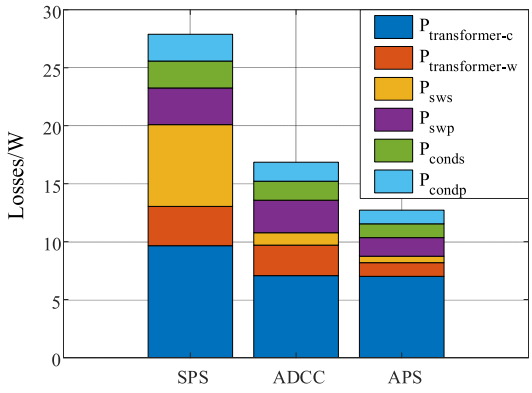

Fig. 19. Comparison of loss breakdown with SPS control, APS control, and ADCC control in [28] with $d = 0.6$, $P_n = 0.12$ situation.

$$\sigma_1 = \begin{cases} 1, \text{hard} - \text{switching} \\ 0, \text{ZVS turn} - \text{on} \end{cases} \quad \sigma_2 = \begin{cases} 1, \text{hard} - \text{switching} \\ 0, \text{Z CS turn - off} \end{cases}$$

$$\sigma_3 = \begin{cases} 1, \text{hard - switching} \\ 0, \text{soft} - \text{switching} \end{cases} \tag{40}$$

where f_s is the switching frequency, Q_{rr} is the reverse recovery charge, and V_{rr} is the reverse recovery voltage. The rise time t_r and fall time t_f of switching transient and output capacitance C_{oss} can be read from the diagrams or tables in the MOSFET datasheet. V_{DS}, I_{Don}, I_{Doff} can be obtained from characteristic equations related to the converter's operation or from simulation results. The variables σ_1, σ_2, and σ_3 are equal to 0 or 1 according to the specific soft-switching conditions (ZVS turn-ON, ZCS turn-OFF, or hard-switching).

The winding losses of transformer can be calculated for litz wires with considerations of the skin and proximity effect, and winding losses can be calculated using effective winding resistance [30]

$$P_{\text{winding}} = I_{\text{rms}}^2 \cdot \rho \cdot N \cdot l_{\text{wdg}}/n \tag{41}$$

where $I^2{}_{\text{rms}}$ is the rms value of the current, ρ is the effective resistivity of litz wire with considering the skin and proximity effect, l_{wdg} is the length of winding per turn, N is the number of turns, and n represents the number of strands.

The core losses of transformer can be approximately calculated by the improved generalized Steinmetz's equation [31], [32]

$$P_{\text{core\_}T} = V_{\text{core\_}T} \cdot \frac{1}{T_s}\int_0^{T_s} k_i \left|\frac{dB}{dt}\right|^{\alpha} (\Delta B)^{(\beta-\alpha)} dt \tag{42}$$

where the $V_{\text{core\_}T}$ represents the effective volume of the core, T_s represents the switching period, ΔB represents the peak to peak value of flux density, and k_i, α, and β are the coefficients defined by the magnetic core material.

Based on (39)–(42), the total power losses, including the conduction losses of semiconductors, the switching losses of semiconductors, the winding losses of transformer, and the core losses of transformer, can be calculated with $d = 0.6$ and $P_n = 0.12$ situation. Fig. 19 shows the loss distribution in this selected situation by using SPS control, ADCC control in [28], and APS control proposed in this manuscript comparatively, where $P_{\text{transformer-}c}$ represents core losses of transformer, $P_{\text{transformer-}w}$ represents winding losses of transformer, P_{sws}

$$\begin{cases} P_{\text{middle}} = \dfrac{4D_1(d^2-(1+d^2)D_1+\sqrt{D_1(d^2(-1+D_1)+D_1)})}{3d} \\ I_{\text{middle}} = \dfrac{(d^4+32D_1^2(D1-\sqrt{D_1(d^2(-1+D_1)+D_1)})}{18d^2} \\ \quad + \dfrac{4d^2D_1(8\sqrt{D_1\left(d^2\left(-1+D_1\right)+D_1\right)}+D_1\left(-9+8D_1-8\sqrt{D_1\left(d^2\left(-1+D_1\right)+D_1\right)}\right)))\pi^2}{18d^2} \end{cases} \tag{43}$$

represents the switching losses of switches in secondary side, P_{swp} represents the switching losses of switches in primary side, P_{conds} represents the conduction losses of switches in secondary side, and P_{condp} represents the conduction losses of switches in primary side. In Fig. 19, it is concluded that both ADCC control and APS control can reduce transformer losses and semiconductors losses significantly by compared with SPS control. Moreover, APS control will achieve lower switching losses, conduction losses of power switches, and lower winding losses of transformer. These make APS control obtain slightly higher efficiency than ADCC control.

VI. Conclusion

This article proposes a novel control method of 3ph-DAB, known as APS control. This proposed APS method, unlike other control methods proposed in existing literature, controls the phase-shift angles among three-phase legs rather than duty cycles to improve the 3ph-DAB performance. The multifrequency approximation model under the novel APS control is developed to avoid numerous switching states analysis based on this novel control scheme. Further, the optimized modulation strategy is proposed to minimize the 3ph-DAB conduction loss and extend the soft-switching range by utilizing the phase-shift angles among the three-phase legs in the primary and secondary sides as additional degrees of control freedoms. The optimized modulation strategy adopts the interior-point method combined with the Lagrange multiplier method and GOC equation to solve the numerical and analytical solutions of optimal phase-shift angles, respectively. By comparing the conventional SPS control, the proposed APS control achieves a massive reduction in 3ph-DAB conduction and switching losses, particularly at the large voltage variations ratio conditions. Moreover, it provides analytical solutions for optimal phase-shift angles to be convenient for digital control implementation. The novel APS control can be regarded as the unified control method, which includes the conventional SPS and 1ph-DAB controls. The optimal TPS control of the 1ph-DAB converter and conventional SPS control are special cases of APS control under light- and heavy-load conditions, respectively. The proposed modulation schemes and implementation methods are verified by experimental results on a down-scaled 3ph- DAB converter prototype.

Appendix

According to the solution 1, which is shown in the (37) and literature [25], the transferred power and I^2_{rms} expressions under 1ph-DAB mode control at power range $P\in[(d^2-d^3)\pi/3,(-1+d(\sqrt{(}-1+1/d^2)+d))\pi/3d]$ can be listed

According to (43) shown at the top of this page, the I_{middle} can be described as the function that relates to the phase-shift angle D_1. Solving (43), the I_{middle} can be written as function that relates to the transferred power P and voltage ratio d.

References

[1] B. Zhao, Q. Song, W. Liu, and Y. Sun, "Overview of dual-active-bridge isolated bidirectional DC–DC converter for high-frequency-link power-conversion system," *IEEE Trans. Power Electron.*, vol. 29, no. 8, pp. 4091–4106, Aug. 2014.

[2] B. Zhao, Q. Song, W. Liu, and Y. Xiao, "Next-generation multi-functional modular intelligent UPS system for smart grid," *IEEE Trans. Ind. Electron.*, vol. 60, no. 9, pp. 3602–3618, Sep. 2013.

[3] S. P. Engel, M. Stieneker, N. Soltau, S. Rabiee, H. Stagge, and R. W. De Doncker, "Comparison of the modular multilevel DC converter and the dual-active bridge converter for power conversion in HVDC and MVDC grids," *IEEE Trans. Power Electron.*, vol. 30, no. 1, pp. 124–137, Jan. 2015.

[4] H. Wen, W. Xiao, and B. Su, "Nonactive power loss minimization in a bidirectional isolated DC–DC converter for distributed power systems," *IEEE Trans. Ind. Electron.*, vol. 61, no. 12, pp. 6822–6831, Dec. 2014.

[5] M. N. Kheraluwala, R. W. Gascoigne, D. M. Divan, and E. D. Baumann, "Performance characterization of a high-power dual active bridge DC-to-DC converter," *IEEE Trans. Ind. Appl.*, vol. 28, no. 6, pp. 1294–1301, Nov. 1992.

[6] J. Hu, P. Joebges, G. C. Pasupuleti, N. R. Averous, and R. W. De Doncker, "A maximum-output-power-point-tracking-controlled dual-active bridge converter for photovoltaic energy integration into MVDC grids," *IEEE Trans. Energy Convers.*, vol. 34, no. 1, pp. 170–180, Mar. 2019.

[7] S. P. Engel, N. Soltau, H. Stagge, and R. W. De Doncker, "Improved instantaneous current control for high-power three-phase dual-active bridge DC–DC converters," *IEEE Trans. Power Electron.*, vol. 29, no. 8, pp. 4067–4077, Aug. 2014.

[8] J. Hu, S. Cui, S. Wang, and R. W. De Doncker, "Instantaneous flux and current control for a three-phase dual-active bridge DC–DC converter," *IEEE Trans. Power Electron.*, vol. 35, no. 2, pp. 2184–2195, Feb. 2020.

[9] Z. Li, Y. Wang, Y. Cui, L. Shi, J. Huang, and W. Lei, "Fast transient current control for three-phase dual-active-bridge dc-dc converters with variable duty cycles," in *Proc. IEEE Appl. Power Electron. Conf. Expo.*, 2017, pp. 1209–1215.

[10] R. W. A. A. De Doncker, D. M. Divan, and M. H. Kheraluwala, "A three-phase soft-switched high-power-density DC/DC converter for high-power applications," *IEEE Trans. Ind. Appl.*, vol. 27, no. 1, pp. 63–73, Jan./Feb. 1991.

[11] F. Krismer and J. W. Kolar, "Closed form solution for minimum conduction loss modulation of DAB converters," *IEEE Trans. Power Electron.*, vol. 27, no. 1, pp. 174–188, Jan. 2012.

[12] N. Hou and Y. W. Li, "Overview and comparison of modulation and control strategies for a nonresonant single-phase dual-active-bridge DC–DC converter," *IEEE Trans. Power Electron.*, vol. 35, no. 3, pp. 3148–3172, Mar. 2020.

[13] H. van Hoek, M. Neubert, and R. W. De Doncker, "Enhanced modulation strategy for a three-phase dual active bridge—Boosting efficiency of an electric vehicle converter," *IEEE Trans. Power Electron.*, vol. 28, no. 12, pp. 5499–5507, Dec. 2013.

[14] G.-J. Su and L. Tang, "A three-phase bidirectional DC-DC converter for automotive applications," in *Proc. IEEE Ind. Appl. Soc. Annu. Meeting*, 2008, pp. 1–7.

[15] Z. Li, Y. Wang, L. Shi, J. Huang, and W. Lei, "Optimized modulation strategy for three-phase dual-active-bridge DC-DC converters to minimize RMS inductor current in the whole load range," in *Proc. IEEE 8th Int. Power Electron. Motion Control Conf.*, 2016, pp. 2787–2791.

[16] J. Huang, Z. Li, L. Shi, Y. Wang, and J. Zhu, "Optimized modulation and dynamic control of a three-phase dual active bridge converter with variable

duty cycles," *IEEE Trans. Power Electron.*, vol. 34, no. 3, pp. 2856–2873, Mar. 2019.
[17] L. M. Cúnico, Z. M. Alves, and A. L. Kirsten, "Efficiency-optimized modulation scheme for three-phase dual-active-bridge DC–DC converter," *IEEE Trans. Ind. Electron.*, vol. 68, no. 7, pp. 5955–5965, Jul. 2021.
[18] J. Huang, Y. Wang, Z. Li, and W. Lei, "Multifrequency approximation and average modelling of an isolated bidirectional dc–dc converter for dc microgrids," *IET Power Electron.*, vol. 9, no. 6, pp. 1120–1131, 2016.
[19] S. P. Boyd and L. Vandenberghe, *Convex Optimization*. Cambridge, U.K.: Cambridge Univ. Press, 2004.
[20] R. A. Waltz, J. L. Morales, J. Nocedal, and D. Orban, "An interior algorithm for nonlinear optimization that combines line search and trust region steps," *Math. Program.*, vol. 107, no. 3, pp. 391–408, Jul. 2006.
[21] B. Liu, Q. Yang, H. Zhang, and H. Wu, "An interior-point solver for AC optimal power flow considering variable impedance-based FACTS devices," *IEEE Access*, vol. 9, pp. 154460–154470, 2021.
[22] B. V. Rao, G. V. N. Kumar, R. V. S. L. Kumari, and N. G. S. Raju, "Optimization of a power system with interior point method," in *Proc. Int. Conf. Power Energy Syst.*, Dec. 2011, pp. 1–6.
[23] Y. Huping, G. Yin, Z. Yang, and B. Zhipeng, "Reactive power optimization of power system based on interior point method and branch-bound method," in *Proc. 2nd Int. Conf. Power Electron. Intell. Transp. System*, Dec. 2009, vol. 3, pp. 5–8.
[24] Y. Zhao and Q. Liu, "A lagrange multiplier method for distributed optimization based on multi-agent network with private and shared information," *IEEE Access*, vol. 7, pp. 83297–83305, 2019.
[25] A. Tong, L. Hang, G. Li, X. Jiang, and S. Gao, "Modeling and analysis of a dual-active-bridge-isolated bidirectional DC/DC converter to minimize RMS current with whole operating range," *IEEE Trans. Power Electron.*, vol. 33, no. 6, pp. 5302–5316, Jun. 2018.
[26] A. Tong, L. Hang, and G. Li, "Optimized control strategy for minimum ohmic loss of dual acitve bridge converter," in *Proc. IEEE Appl. Power Electron. Conf. Expo.*, 2017, pp. 1103–1110.
[27] J. Huang, Y. Wang, Z. Li, and W. Lei, "Unified triple-phase-shift control to minimize current stress and achieve full soft-switching of isolated bidirectional DC–DC converter," *IEEE Trans. Ind. Electron.*, vol. 63, no. 7, pp. 4169–4179, Jul. 2016.
[28] J. Hu, Z. Yang, S. Cui, and R. W. De Doncker, "Closed-form asymmetrical duty-cycle control to extend the soft-switching range of three-phase dual-active-bridge converters," *IEEE Trans. Power Electron.*, vol. 36, no. 8, pp. 9609–9622, Aug. 2021.
[29] X. Pan, H. Li, Y. Liu, T. Zhao, C. Ju, and A. K. Rathore, "An overview and comprehensive comparative evaluation of current-fed-isolated-bidirectional DC/DC converter," *IEEE Trans. Power Electron.*, vol. 35, no. 3, pp. 2737–2763, Mar. 2020.
[30] F. Tourkhani and P. Viarouge, "Accurate analytical model of winding losses in round litz wire windings," *IEEE Trans. Magn.*, vol. 37, no. 1, pp. 538–543, Jan. 2001.
[31] N. Soltau, D. Eggers, K. Hameyer, and R. W. De Doncker, "Iron losses in a medium-frequency transformer operated in a high-power DC–DC converter," *IEEE Trans. Magn.*, vol. 50, no. 2, pp. 953–956, Feb. 2014.
[32] K. Venkatachalam, C. R. Sullivan, T. Abdallah, and H. Tacca, "Accurate prediction of ferrite core loss with nonsinusoidal waveforms using only steinmetz parameters," in *Proc. IEEE Workshop Comput. Power Electron.*, 2002, pp. 36–41.
[33] N. Hou, Y. Zhang, and Y. W. Li, "A load-current-estimating scheme with delay compensation for the dual-active-bridge DC–DC converter," *IEEE Trans. Power Electron.*, vol. 37, no. 3, pp. 2636–2647, Mar. 2022.
[34] N. Hou and Y. W. Li, "Overview and comparison of modulation and control strategies for a nonresonant single-phase dual-active-bridge DC–DC converter," *IEEE Trans. Power Electron.*, vol. 35, no. 3, pp. 3148–3172, Mar. 2020.

Hui Chen (Student Member, IEEE) received the B.S. degree in electrical engineering and automation from Dalian Maritime University, Dalian, China, in 2016, and the M.S. degree in electrical engineering in 2019 from the School of Electrical Engineering, Xi'an Jiaotong University, Xi'an, China, where he is currently working toward the Ph.D. degree in electrical engineering with Xi'an Jiaotong University, Xi'an China.

His current research interests include power electronic transformer, bidirectional isolated dc–dc converters topology and control techniques.

Shaodi Ouyang (Member, IEEE) received the B.S. degree in electrical engineering from the Huazhong University of Science and Technology, Wuhan, China, in 2011, and the Ph.D degree in electrical engineering from Xi'an Jiaotong University, Xi'an, China, in 2018.

From 2019 to 2021, he was a Postdoctoral Research Associate with Xi'an Jiaotong University. He joined the HuaWei Technologies Company Ltd., in 2021. His research interests include power electronic transformer, multilevel converters and dc/dc converters.

Jinjun Liu (Fellow, IEEE) received the B.S. and Ph.D. degrees in electrical engineering from Xi'an Jiaotong University (XJTU), Xi'an, China, in 1992 and 1997, respectively.

He then joined the XJTU Electrical Engineering School as a Faculty. From late 1999 to early 2002, he was with the Center for Power Electronics Systems, Virginia Polytechnic Institute and State University, Blacksburg, VA, USA, as a Visiting Scholar. In late 2002, he was promoted to a Full Professor and then the Head of the Power Electronics and Renewable Energy Center, XJTU, which now comprises more than 20 faculty members and more than 200 graduate students and carries one of the leading power electronics programs in China. From 2005 to early 2010, he was as an Associate Dean of Electrical Engineering School, XJTU, and from 2009 to early 2015, he was the Dean for Undergraduate Education of XJTU. He is currently an XJTU Distinguished Professor of power electronics. He has coauthored three books (including one textbook), authored or coauthored more than 500 technical papers in peer-reviewed journals and conference proceedings, holds 70 invention patents (China/US/EU), and delivered for many times plenary keynote speeches and tutorials at the IEEE conferences or China national conferences. His research interests include modeling, control, and design methods for power converters and electronified power systems, power quality control and utility applications of power electronics, and microgrids for sustainable energy and distributed generation.

Dr. Liu was the recipient for many times governmental awards at national level or provincial/ministerial level for scientific research/teaching achievements, 2006 Delta Scholar Award, 2014 Chang Jiang Scholar Award, 2014 Outstanding Sci-Tech Worker of the Nation Award, 2016 State Council Special Subsidy Award, IEEE TRANSACTIONS ON POWER ELECTRONICS 2016 and 2021 Prize Paper Awards, and the Nomination Award for the Grand Prize of 2020 Bao Steel Outstanding Teacher Award. He was the IEEE Power Electronics Society Region 10 Liaison and then China Liaison for ten years, has been an Associate Editor for the IEEE TRANSACTIONS ON POWER ELECTRONICS since 2006, 2015–2019 Executive Vice President, and 2020–2021 Vice President of IEEE PELS. He was on the Board of China Electrotechnical Society in 2012–2020 and was elected the Vice President in 2013 and the Secretary General in 2018 of the CES Power Electronics Society. He was the Vice President for International Affairs, China Power Supply Society (CPSS) from 2013 to 2021, and since 2016, he has been the inaugural Editor-in-Chief of *CPSS Transactions on Power Electronics and Applications*. He was elected the President of CPSS in November 2021. Since 2013, he has been the Vice Chair of the Chinese National Steering Committee for College Electric Power Engineering Programs.

Xianzao Li (Student Member, IEEE) received the B.E. degree in electrical engineering and automation from Xi'an Jiaotong University, Xi'an, China, in 2020. He is currently working toward the M.Sc. degree in control and optimisation from Imperial College London, London, U.K.

His current research interests include wireless power transfer, power electronic transformer, bidirectional isolated dc–dc converters, and control techniques.